Numerical study of frost formation in a membrane for HVAC applications

A Thesis Submitted to the College of Graduate and Postdoctoral Studies

In Partial Fulfillment of the Requirements

For the Degree of Master of Science

In the Department of Mechanical Engineering

University of Saskatchewan

Saskatoon

By

Pooya Navid

PERMISSION TO USE

In presenting this thesis in partial fulfillment of the requirements for a Postgraduate degree from the University of Saskatchewan, I agree that the Libraries of this University may make it freely available for inspection. I further agree that permission for copying of this thesis in any manner, in whole or in part, for scholarly purposes may be granted by the professor or professors who supervised my thesis work or, in their absence, by the Head of the Department or the Dean of the College in which my thesis work was done. It is understood that any copying or publication or use of this thesis or parts thereof for financial gain shall not be allowed without my written permission. It is also understood that due recognition shall be given to me and to the University of Saskatchewan in any scholarly use which may be made of any material in my thesis.

Requests for permission to copy or to make other use of material in this thesis in whole or part should be addressed to:

Head of the Department of Mechanical Engineering
57 Campus Drive
University of Saskatchewan
Saskatoon, Saskatchewan (S7N 5A9)
Canada

OR

Dean
College of Graduate and Postdoctoral Studies
University of Saskatchewan
116 Thorvaldson Building, 110 Science Place
Saskatoon, Saskatchewan (S7N 5C9)
Canada

ABSTRACT

In this thesis, a numerical model for heat and mass transfer in a membrane is developed to identify the onset of saturation (frosting) in the membrane and verified. The numerical model is a porous media model based on the theory of local volume averaging and local thermal equilibrium and determines the temperature and relative humidity profiles inside the membrane in order to show the location and time of saturation. Warm and humid air flows above the membrane and cold liquid desiccant flows below the membrane. The goal of this research is to determine how to avoid saturation conditions through the membrane because saturation is essential for frosting. The numerical model is validated with experimental data and shows that frost formation can be prevented or delayed by controlling the moisture transfer rate through the membrane which is a new idea and thus a contribution to the research literature.

The results of the numerical model show that the temperature and humidity profiles inside the membrane are linear at steady-state conditions. Therefore, an analytical model based on thermal and mass resistances is used to accurately predict the temperature and relative humidity at the top and bottom surfaces of the membrane under steady-state conditions. The analytical model is verified with experimental and numerical data at steady-state conditions. With the analytical model, the conditions that result in saturation conditions can be determined by directly solving two algebraic equations.

The numerical and analytical models are also used to determine the sensitivity of several parameters on the time and location of saturation, including: the vapor diffusion coefficient, the heat and mass transfer coefficients, the thickness of the membrane, the liquid desiccant concentration, and the thermal conductivity of the membrane.

ACKNOWLEDGEMENTS

I would like to express my appreciation to my supervisor, Professor Carey J. Simonson, for his support and advice throughout my research. I have learned many professional and personal life lessons.

Special thanks go to Shirin Niroomand for her support and useful discussions during my research. I would also like to thank my colleagues Mohamed R.H. Abdel-Salam, Adesola Olufade, Devin Storle, Gaoming Ge, Mohammad Rafati Nasr, Farhad Fathieh, Ahmed Abdel-Salam, Houman Kamali, Melanie Fauchoux, and Shawn Reinink for their support during my research.

This research was financially supported by the Natural Science and Engineering Research Council of Canada (NSERC) and the College of Graduate and Postdoctoral Studies at University of Saskatchewan.

DEDICATION

I dedicate this thesis to my family, Saba, Shayesteh, and Daryoush.

TABLE OF CONTENTS

LIST OF TABLES

Table **Page**

LIST OF FIGURES

Figure **Page**

NOMENCLATURE

Acronyms

HVAC	heating, ventilation, and air conditioning
IAQ	indoor air quality
LAMEE	liquid-to-air membrane energy exchanger
LTE	local thermal equilibrium
LVA	local volume averaging
RAMEE	run-around membrane energy exchanger
REV	representative elementary volume
TC	thermocouple

English Symbols

B	systematic uncertainty, $(-)$
c_p	specific heat, J/(kg·K)
C	concentration, %
d	diameter of membrane fibers, m
D	diffusion coefficient for water vapor in air, m^2/s
D_{AB}	binary diffusion coefficient for water vapor in air, m^2/s
err	error
eqv	equivalent
h_{fg}	evaporation specific enthalpy of saturated liquid water, J/kg
h_m	local convective mass transfer coefficient, m/s
h_h	heat transfer coefficient, $W/(m^2 \cdot K)$
k	thermal conductivity, W/(m·K)
l	representative elementary volume of characteristic length, m
L	thickness of membrane, m
L_T	characteristic length, m
Le	Lewis Number, $(-)$
$\dot{m}$	phase change rate, $kg/(s \cdot m^3)$
Nu	Nusselt Number, $(-)$
P	pressure or random uncertainty, Pa or $(-)$
q	flux, (W/m^2) or $(kg/(m^2 s))$
R	specific gas constant, J/(kg·K)
R_h	thermal resistance, $(K \cdot m^2)/W$
R_m	moisture resistance, s/m

Ra	Rayleigh Number, $(-)$
RH	relative humidity, %
t	time, s
T	temperature, ℃
u	mass of moisture adsorbed per kg of dry membrane, kg/kg
U	total uncertainty, $(-)$
W	humidity ratio of air, g_v/kg_a
x	length direction perpendicular to the membrane, m

Greek Symbols

α	dimensionless properties, $(-)$
ΔDP	allowable dew point depression of the surface, ℃
ε	volume fraction, $(-)$
ρ	density, kg/m^3
τ	tortuosity coefficient, $(-)$
φ	different properties

Subscript

anl	analytical
eff	effective
err	error
exp	experimental
g	gas
h	heat
l	liquid
LD	liquid desiccant
m	moisture
mem	membrane
num	numerical
sat	saturation
$sens$	sensitivity
sol	solution
tot	total
v	water vapor

Superscript

$*$	dimensionless quantity

Chemical Symbols

$LiCl$	lithium chloride

CHAPTER 1

INTRODUCTION

1.1 Motivation

World population is increasing rapidly. The world had 2.5 billion people in 1950, and 6.5 billion people in 2005. By 2050, this world population could increase to more than 9.8 billion (UN Population Division, 2017). Since people consume resources like food, water, fuel, world energy consumption is expected to grow by about 50% between 2012 and 2040 (Energy Information Administration (EIA), 2016). Growing population and energy demand are expected to increase energy cost, air pollution, water pollution, and climate change. Studies show that about 40% of energy consumption in North America is consumed in residential and commercial buildings (Energy Information Administration (EIA), 2016). About 55% of this energy is used by heating, ventilation and air conditioning (HVAC) systems to provide comfort for the occupants in buildings. In 2013, Canadians spent almost $195 billion on energy to heat and cool their homes and offices (Natural Resources Canada, 2013). Therefore, many researchers and engineers focus on reducing the energy consumption of HVAC systems. One method to reduce HVAC energy consumption is to implement energy recovery systems. Membrane-based energy exchangers are a new component of energy recovery systems and are the focus of this thesis.

Although using membrane energy exchangers has become more popular in the past few years, implementing them in cold climates like Canada is a challenge, because the exchangers are vulnerable to frosting which can significantly reduce their performance (Alonso et al., 2017). Therefore, there is a high demand for developing frost-free exchangers. In order to develop a frost-free energy exchanger, a physical understanding and accurate analysis of frost initiation in membranes are essential. The main goal of this study is to develop a model to investigate if moisture transfer through membranes can delay or prevent frost formation.

1.2 Background

The goal of an HVAC system is to provide thermal comfort and acceptable indoor air quality (IAQ). HVAC systems play an important role in our daily life because people spend the majority

of their time inside buildings. Thermal comfort involves control of temperature, humidity, and air motion. HVAC systems adjust temperature and humidity to provide thermal comfort for occupants. Additionally, HVAC systems remove air contaminants by providing fresh air to maintain an acceptable indoor air quality (IAQ). IAQ is related to chemical and particle composition of air and affects the health and productivity of occupants.

HVAC systems consume a lot of energy to provide comfort and good IAQ for building occupants. Recovery systems can notably reduce the energy needed to cool and heat ventilation air by transferring energy between the incoming ventilation air and outgoing exhaust air. Therefore, the ventilation air supplied to the building becomes preconditioned closer to the indoor conditions. Exchangers, fans, filters, and control system as one unit is called heat/energy recovery systems. Membrane energy exchangers can transfer heat and moisture simultaneously between the supply and exhaust air streams. The membrane exchanger cools and dries the supply air in the summer and heats and humidifies the supply air in the winter. Membranes can be implemented in air-to-air membrane energy exchangers (Section 1.2.1) and liquid-to-air membrane energy exchanger (LAMEE) (Section 1.2.2).

1.2.1 Air-to-air membrane energy exchanger

An air-to-air membrane energy exchanger is a membrane energy exchanger that transfers heat and moisture between the return air and exhaust air in energy recovery systems. The technology is cost effective and reduces energy consumption in the HVAC systems. Rafati Nasr (2016) experimentally showed that using permeable membranes delays frost formation in air-to-air membrane energy exchangers about 5℃ to 10℃ compared with an impermeable plate under the same air flow rate and exhaust air relative humidity. Liu (2016) developed a simplified theoretical model to predict conditions under which frost will form in the air-to-air permeable membrane energy exchanger and air-to-air impermeable plate heat exchanger. The model used the exchanger design parameters and operating conditions to determine the frosting limit.

1.2.2 Liquid-to-air membrane energy exchanger (LAMEE)

A LAMEE is a membrane energy exchanger which transfers heat and moisture simultaneously between an air stream and a liquid desiccant through permeable membranes. LAMEEs can be implemented in energy recovery systems as active air dehumidification and humidification

systems (Abdel-Salam, 2015). Figure 1.1 shows two LAMEE prototypes and Figure 1.2 shows a schematic of a run-around membrane energy exchanger (RAMEE) composed of two LAMEEs.

Figure 1.1: Photograph of the two fully assembled LAMEEs (Erb, 2009).

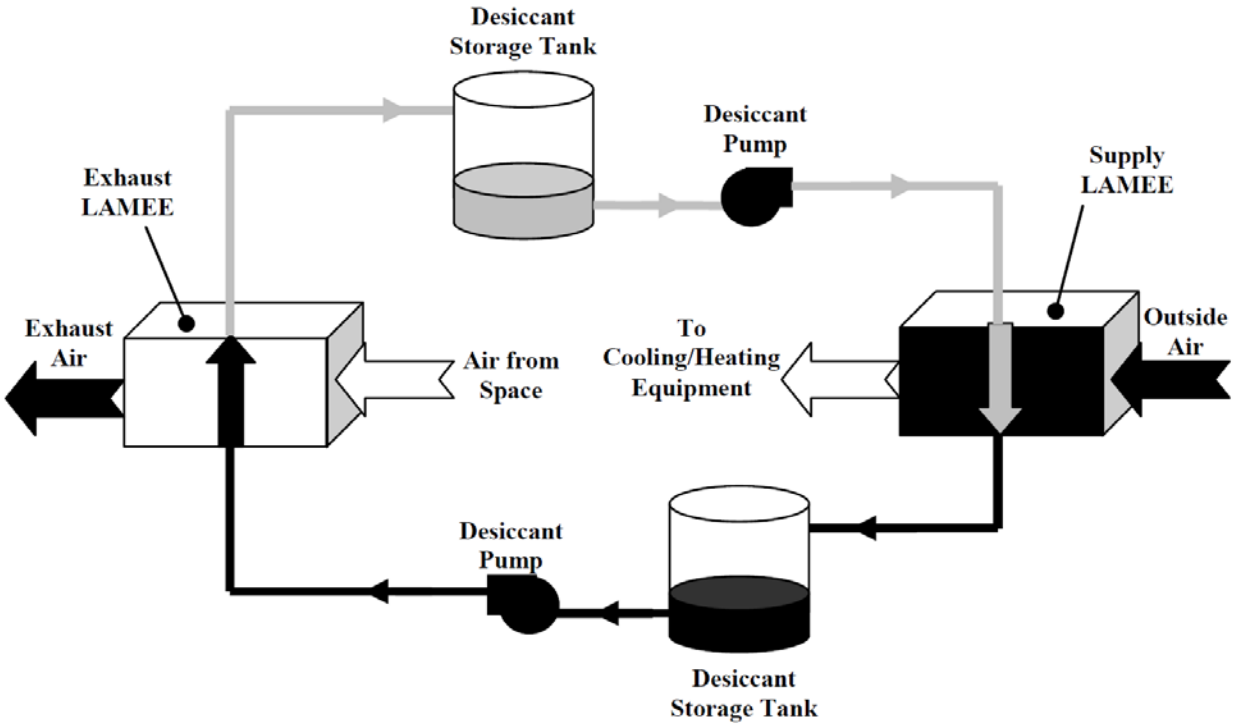

Figure 1.2: Schematic of a RAMEE (Erb, 2009).

1.2.3 Saturation

Many researchers have tried to avoid frost formation using defrosting techniques like heating, anti-icing chemicals and surface modification especially hydrophobic surfaces (Kim et al., 2016; Sommers et al., 2016; Rahimi et al., 2015; Oberli et al., 2014; Na and Webb, 2003; Parent and Ilinca, 2011). The focus of this thesis is frosting in membrane energy exchangers. Before frosting can occur, the air in the membrane energy exchanger must become saturated (Borgnakke and Sonntag, 2012) and the membrane must be below 0°C. Saturation occurs when the temperature is less than or equal to the dew point temperature (i.e., the relative humidity equals 100%) as labeled on the psychrometric chart in Figure 1.3. The process of cooling air from state point (A) to saturation which results in condensation is shown in Figure 1.3. Further cooling of the air results in freezing or frosting. When the air contacts a cold surface, its temperature decreases. If the surface temperature is below the dew point, condensation occurs. If the temperature is below the freezing point, freezing occurs.

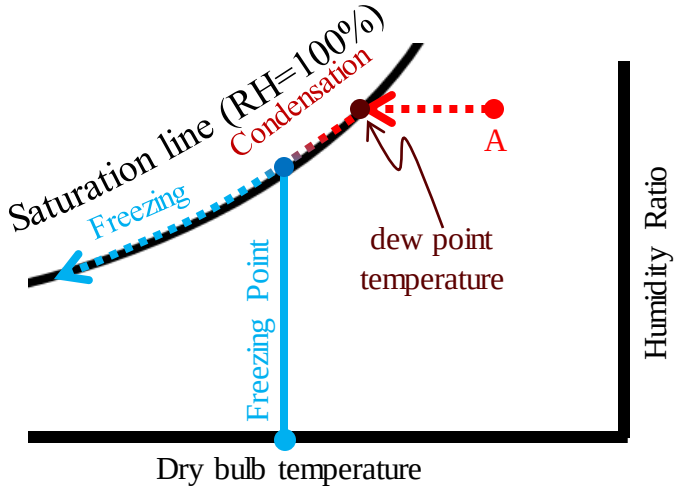

Figure 1.3: Psychrometric chart shows air condenses and then freezes in contact with a cold surface.

Since saturation is a prerequisite for frosting, this thesis will focus on avoiding saturation conditions which will eliminate frosting.

1.3 Objectives

As mentioned earlier, moisture transfer through a membrane may reduce the risk of frosting in energy exchangers. The hypothesis of this research is that it is feasible to achieve a frost-free

exchanger with a vapor permeable membrane. This hypothesis will be tested in this research which is divided into the following objectives:

1. Develop a numerical model for heat and moisture transfer in a vapor permeable membrane to determine when the air in the membrane becomes saturated,
2. Verify the numerical model with experimental data,
3. Investigate the effects of design and operating parameters on the onset of saturation in the membrane.

1.4 Thesis Structure

The thesis is a manuscript-style thesis containing two research papers (chapters 2 and 3) that address the objectives of the thesis. The first two objectives are addressed in chapter 2 where a numerical model is developed and verified. Chapter 3 addresses the third objective of the thesis which is to investigate the effects of different parameters on avoiding saturation (or preventing frosting). Chapter 4 presents a summary of the thesis, conclusions, and recommendations for future work.

The Appendixes contain supplemental information. Appendix A summarizes the local volume averaging and local thermal equilibrium techniques which are used to develop the numerical model. Appendix B presents the discretized equations and the computer simulation program. Appendix C presents the investigation of the reliability of the grid size, time step, convergence, and residuals of the computer simulation program. In Appendix D, the numerical model is verified with an analytical solution.

1.5 List of publications

The following papers are included as chapters in this thesis. Both papers have been submitted for publication and are currently under review.

Chapter 2: Navid P., Niroomand S., Simonson C.J., 2018. A new approach to delay or prevent frost formation in membranes. ASME Journal of Heat Transfer, Submitted.

Chapter 3: Navid P., Niroomand S., Simonson C.J., 2018. Theoretical model for predicting frosting limit in membranes. International Journal of Refrigeration, Submitted.

CHAPTER 2

NUMERICAL MODEL

2.1 Overview of Chapter 2

The goal of this thesis is to determine if moisture transfer through a vapor permeable membrane can avoid and delay frosting in energy exchangers. The objective of this chapter is to develop a numerical model to calculate temperature and humidity profiles within a membrane and determine when and where saturation occurs. The model is verified with experimental data and used to show the effect of different parameters on saturation. The results show that moisture transfer through the membrane delays saturation and frosting. As the moisture transfer rate through the membrane increases, the delay in saturation (and frosting) increases.

The manuscript presented in this chapter has been submitted to the ASME Journal of Heat Transfer. The three authors are Pooya Navid (MSc student) who performed the study and wrote the manuscript, Shirin Niroomand (PhD student) who reviewed the manuscript, wrote Section 2.6, and developed the experimental facility, and Carey J. Simonson (MSc supervisor who reviewed the manuscript and supervised the study).

A new approach to delay or prevent frost formation in membranes

Pooya Navid, Shirin Niroomand, Carey J. Simonson

2.2 Abstract

Saturation of the water vapor is essential to form frost inside a permeable membrane. The main goal of this chapter is to develop a numerical model that can predict temperature and humidity inside a membrane in order to show the location and time of saturation. This numerical model for heat and moisture transfer is developed to show that frost formation may be prevented or delayed by controlling the moisture transfer through the membrane which is the new approach in this chapter. The idea is to simultaneously dry and cool air to avoid saturation conditions and thereby eliminate condensation and frosting in the membrane. Results show that saturation usually occurs on side of the membrane with the highest temperature and humidity. The numerical model is verified with experimental data and used to show that moisture transfer through the membrane can delay or prevent frost formation.

2.3 Introduction

In cold climates like Canada and Northern Europe, there is a high risk of frost formation in energy exchangers. Frosting occurs when the warm and humid air flowing through the exchangers cools below the frosting point and the water vapor in the air changes phase and forms crystals on the surface that separates the two airstreams. It is important to note that saturation is a prerequisite for phase change (frosting or condensation) (Borgnakke and Sonntag, 2012). The frost layer acts like an insulation layer that reduces heat and moisture transfer between the two streams. Frost formation significantly reduces the performance of the exchangers and HVAC (Heating, Ventilation and Air Conditioning) systems (Amer and Wang, 2017; Liu et al., 2016; Léoni et al., 2016). Frost formation has negative effects in many industrial applications such as refrigeration, compressor blades, aircraft wings, wind turbines, heat pumps and heat recovery systems which were studied in the literature (Kim et al., 2012; Hong et al., 2014; Amer and Wang, 2017; Li et al., 2017).

There are many studies on frost formation on impermeable surfaces. Many studies focus on reducing or removing frost through heating, anti-icing chemicals and surface modification

especially hydrophobic surfaces (Jeong et al., 2016; Kim et al., 2016; Sommers et al., 2016; Rahimi et al., 2015; Oberli et al., 2014; Na and Webb, 2003; Parent and Ilinca, 2011). Other studies have shown that moisture transfer reduces the risk of frosting in energy wheels which are rotating energy exchangers (Shang et al., 2005; Mahmood and Simonson, 2012). Moreover, experimental studies have shown that the performance of membrane energy exchangers under frosting operating conditions is generally better than the performance of sensible heat exchangers (Alonso et al., 2017; Rafati Nasr et al., 2015; Liu et al., 2016). However, these experimental studies were on an entire exchanger and therefore the conditions within the membrane were not measured. Detailed studies of a membrane under frosting operating conditions have not been presented in the literature. Furthermore, most numerical studies about frost are related to frost growth on impermeable plates (Léoni et al., 2016; Wu et al., 2016; Negrelli et al., 2016; Zhuang et al., 2015). This chapter contributes to the literature by using a numerical study to provide understanding of frosting in membranes for energy exchangers.

The main objective of this chapter is to investigate the possibility of delaying or preventing saturation (which is required for frost formation) in membrane exchangers by controlling moisture transfer through the membrane. The idea is to simultaneously dry and cool the air in contact with the membrane to avoid saturation conditions and thereby eliminate condensation and frosting. Therefore, this new approach to avoiding frosting can prevent frost formation in permeable membranes not only for HVAC applications, but also any other applications which use vapor permeable membranes.

2.4 Physical Model

To describe the physical problem, a cross section of a membrane is shown in Figure 2.1. The properties of the membrane (Propore™) and an impermeable plastic plate studied in this chapter are presented in Table 2.1. Propore™ is a two-layer composite material consisting of a microporous polypropylene membrane that is laminated to a non-woven polypropylene fabric. The fabric creates a rhombus texture with large opening on the membrane (the darks rhombuses in Figure 2.2 shows the membrane surface and light parts are fabric). Warm and humid air flows over the top of the membrane/plate and cold liquid desiccant passes under the bottom of the membrane/plate. The heat and moisture transfer are assumed to be one-dimensional because the length and the width of the membrane/plate are much greater than the thickness.

Three cases are investigated in this chapter:

1. Permeable membrane
2. Impermeable membrane
3. Impermeable plate

In the case of a permeable membrane, convection heat and moisture transfer occurs between the permeable membrane and the fluids flowing over the top and bottom of the permeable membrane. There is pure heat conduction and diffusion of water vapor through the permeable membrane. In the case of an impermeable membrane, is the same as the permeable membrane except the bottom surface of the membrane is impermeable to moisture transfer. Therefore, there is diffusion of water vapor through the impermeable membrane from the top surface, but water vapor cannot pass through the bottom surface. This second case is selected to investigate the effect of sorption on the initiation of saturation (or frost). The case of an impermeable plate considers an impermeable plate with the same thickness of the membrane. In this case, there is only heat transfer between the plate and the fluids flowing over the top and bottom of the plate and one-dimensional heat conduction through the plate. For all cases, the sides of the membrane/plate are assumed impermeable and adiabatic.

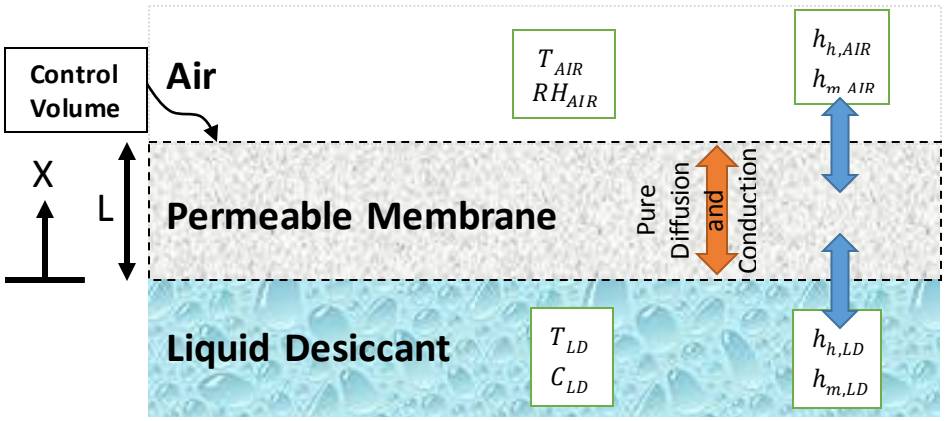

Figure 2.1: Schematic of the problem of heat and moisture transfer through a membrane separating air and liquid desiccant.

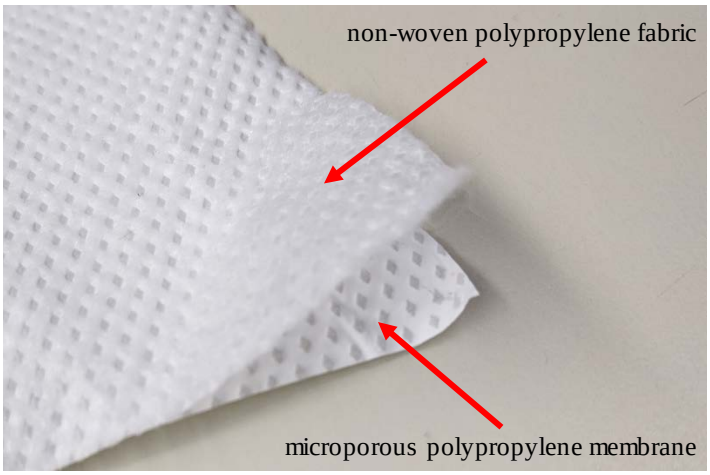

Figure 2.2: Propore™ membrane.

Table 2.1: Base properties of the permeable and impermeable membrane, and impermeable plate used in the numerical simulation.

Properties	Permeable membrane	Impermeable membrane	Impermeable plate
Density	394 kg/m^3	394 kg/m^3	910 kg/m^3
Specific heat	1799 J/(kg·K)	1799 J/(kg·K)	2300 J/(kg·K)
Thermal conductivity	0.34 W/(m·K)	0.34 W/(m·K)	0.35 W/(m·K)
Porosity	0.55 (-)	0.55 (-)	0 (-)
Vapor diffusion coefficient	1.46×10^{-6} m^2/s (Ge et al., 2014)	1.46×10^{-6} m^2/s (Ge et al., 2014)	0 m^2/s
Thickness	200 µm (Ge et al., 2014)	200 µm (Ge et al., 2014)	200 µm
$h_{m,LD}$	∞ m/s (Hemingson, 2010)	0 m/s	0 m/s
$h_{m,AIR}$	5×10^{-3} kg/m^2	5×10^{-3} kg/m^2	0 kg/m^2

2.5 Numerical Model

To find the location of saturation inside the membrane, a porous media model based on the theory of local volume averaging and local thermal equilibrium is used (details are presented in Appendix A). The model solves the temperature and vapor density profiles in a membrane to determine when and where saturation conditions occur. The model is used to determine saturation conditions within the membrane because saturation conditions are a prerequisite for frosting to occur. Therefore, if

moisture transfer avoids saturation condition throughout the membrane, frosting (phase change) can be avoided. Some assumptions were made to simplify the calculations.

1. The total gas pressure is constant.
2. The mass transfer through the membrane is by diffusion only.
3. The air-water vapor moisture behaves like a perfect gas.
4. The porous membrane is homogenous.
5. No chemical reactions occur in the porous membrane other than the phase change due to adsorption.
6. The thermophysical properties of the fluid and air are assumed to be constant.

2.5.1 Governing Equations

The governing equations needed to calculate the temperature and relative humidity in the membrane are presented in this section. The control volume is defined around the membrane as shown in Figure 2.1. Fundamental equations of conservation of energy and mass are given below (Talukdar et al., 2008).

2.5.1.1 Energy Equation

$$\left(\rho c_p\right)_{eff}\frac{\partial T}{\partial t}+\dot{m}h_{fg}=\frac{\partial}{\partial x}\left(k_{eff}\frac{\partial T}{\partial x}\right) \tag{2.1}$$

2.5.1.2 Water Vapor Diffusion Equation

$$\frac{\partial\left(\varepsilon_g\rho_v\right)}{\partial t}-\dot{m}=\frac{\partial}{\partial x}\left(D_{eff}\frac{\partial\rho_v}{\partial x}\right) \tag{2.2}$$

where D_{eff} is the effective diffusion coefficient of the membrane and is related to binary diffusion coefficient for water vapor in air and the tortuosity (τ) of the membrane, as follows:

$$D_{eff}=\frac{\varepsilon_g D_{AB}}{\tau} \tag{2.3}$$

2.5.1.3 Continuity Equation

$$\frac{\partial \varepsilon_l}{\partial t} + \frac{\dot{m}}{\rho_l} = 0 \tag{2.4}$$

2.5.1.4 Moisture Adsorption Equation

The phase change rate ($\dot{m}$) which is related to adsorption is calculated from Equation (2.5) and is a function of the moisture content (u) of the membrane which is presentenced in Equation (2.6).

$$\dot{m} = \frac{\partial u}{\partial t} \rho_{eff,dry} \tag{2.5}$$

where the moisture content (u) for Tyvek® membrane (which is expected to be similar to Propore™) can be found in Iskra (2007).

$$u = 0.0303RH^3 - 0.02938RH^2 + 0.01629RH \tag{2.6}$$

2.5.1.5 Volumetric Constraint Equation

$$\varepsilon_g + \varepsilon_l + \varepsilon_{mem} = 1 \tag{2.7}$$

2.5.2 Physical Properties

The physical properties of the membrane change due to changes in the moisture content and temperature and are calculated as follows:

$$\rho_{eff} = \varepsilon_g (\rho_v + \rho_{AIR}) + \varepsilon_l \rho_l + \varepsilon_{mem} \rho_{mem} \tag{2.8}$$

$$c_{p_{eff}} = \frac{\varepsilon_g \left(\rho_v c_{p,v} + \rho_{AIR} c_{p,AIR}\right) + \varepsilon_l \rho_l c_{p,l} + \varepsilon_{mem} \rho_{mem} c_{p,mem}}{\rho_{eff}} \tag{2.9}$$

$$k_{eff} = \varepsilon_g \left(\frac{\rho_v k_v + \rho_{AIR} k_{AIR}}{\rho_v + \rho_{AIR}}\right) + \varepsilon_l k_l + \varepsilon_{mem} k_{mem} \tag{2.10}$$

For sensitivity studies, dimensionless properties, c_p^*, ρ^*, u^*, k^*, L^*, and D^* are defined relative to the base case properties in Table 2.1 and Equation (2.11).

$$\alpha^* = \frac{\varphi_{sens}}{\varphi_{base}} \tag{2.11}$$

where, α^* is a general dimensionless property (c_p^*, ρ^*, u^*, k^*, L^*, and D^*), φ_{sens} is the value of the property for the sensitivity study and φ_{base} is the value of property in Table 2.1 and Equation (2.11).

2.5.3 Thermodynamic Relations

The water vapor density in Equation (2.2) can be converted to relative humidity by using the following thermodynamic relations:

$$p_v = R_v \rho_v T \tag{2.12}$$

$$p_{AIR} = R_{AIR}\, \rho_{AIR} T \tag{2.13}$$

$$p_{AIR} = p_g - p_v \tag{2.14}$$

$$RH = \frac{p_v}{p_{sat}} \tag{2.15}$$

2.5.4 Boundary Conditions

As shown in Figure 2.1, the top and bottom of the control volume are in the contact with the air and the liquid desiccant respectively. The sides of the control volume are adiabatic and impermeable. The top $(x = L)$ and bottom $(x = 0)$ boundary conditions are:

$$h_{h,LD}\big(T_{LD} - T(0,t)\big) = -k_{eff} \left.\frac{\partial T}{\partial x}\right|_{x=0} \tag{2.16}$$

$$\rho(0,t) = \rho_{LD} = f(C_{LD}, T_{LD}) \text{ (Fauchoux 2012)} \tag{2.17}$$

$$\left.\frac{\partial \rho_v}{\partial x}\right|_{x=0} = 0 \tag{2.18}$$

$$h_{h,AIR}\left(T(L,t)-T_{AIR}\right)=-k_{eff}\left.\frac{\partial T}{\partial x}\right|_{x=L} \tag{2.19}$$

$$h_{m,AIR}\left(\rho(L,t)-\rho_{AIR}\right)=-D_{eff}\left.\frac{\partial \rho_v}{\partial x}\right|_{x=L} \tag{2.20}$$

The combined natural convection and radiation heat transfer are considered to calculate heat transfer coefficient between the air and the membrane. The heat transfer coefficient for natural convection on a horizontal plate for the air side is calculated from the following equations:

$$Nu_{AIR}=0.52Ra^{0.2} \tag{2.21}$$

$$h_{h,AIR}=\frac{k_{AIR}Nu_{AIR}}{L_T} \tag{2.22}$$

For the bottom of the membrane the heat transfer coefficient is calculated for fully developed laminar ($Re_{LD}\approx 4$) flow in a duct ($Nu_{LD}=3.287$) (Rohsenow et al., 2007) as follows:

$$h_{h,LD}=\frac{k_{LD}Nu_{LD}}{L_T} \tag{2.23}$$

The Chilton-Colburn analogy (Bergman et al., 2011) for heat and mass transfer is used to determine the convection mass transfer coefficients between the membrane and the air and liquid desiccant.

$$\frac{h_h}{h_m}=c_pLe^{2/3} \tag{2.24}$$

For the case of an impermeable membrane with no moisture transfer from the bottom surface (case 2), Equation (2.18) is used. For case 3 (impermeable plate) with no moisture transfer from the bottom and top surface of the surface to the liquid desiccant and the air, Equation (2.18) is used and $h_{m,AIR}=0$ in Equation (2.20), and $D_{eff}=0$ in Equation (2.20).

The properties of the membrane and impermeable plate in Table 2.1 and the temperature, humidity and convective transfer coefficients in Table 2.2 are measured and calculated based on the

experimental tests conducted on the Propore™ membrane and impermeable plate. More details on the experiment will be explained in experiment section (Section 2.6).

2.5.5 Initial Conditions

Initially the membrane and impermeable plate temperature, humidity ratio, and moisture content are assumed to be uniform and in equilibrium with the temperature and humidity ratio of the liquid desiccant.

Table 2.2: Boundary conditions.

Parameters	Unit	Value
Liquid Desiccant		
Temperature (T_{LD})	℃	-10 to -17
Concentration of liquid desiccant (C_{LD})	%	36
Equivalent relative humidity ($Eqv.RH_{LD}$)	%	22
Heat transfer coefficient ($h_{h,LD}$)	W/(m^2·K)	50
Mass transfer coefficient ($h_{m,LD}$)	m/s	∞ (Hemingson, 2010)
Air		
Temperature (T_{AIR})	℃	22
Relative humidity(RH_{AIR})	%	12 & 20
Heat transfer coefficient ($h_{h,AIR}$)	W/(m^2·K)	9
Mass transfer coefficient ($h_{m,AIR}$)	m/s	5×10^{-3}

2.5.6 Solution Scheme

The governing equations are discretized using the finite difference method. A MATLAB code has been developed to solve the governing equations (energy equation, water vapor diffusion equation, continuity equation, moisture adsorption equation). The discretized equations and the computer program are presented in Appendix B. The algorithm used to calculate the temperature and relative humidity can be summarized as follows:

1. Input physical data, including physical properties (thickness, thermal conductivity, density, heat capacity, diffusion coefficient of the selected membrane) and operating conditions (temperature, relative humidity, heat and mass transfer coefficients on both sides of the membrane).
2. Calculate and update the effective properties of the membrane.
3. Calculate the temperature at each node from the energy equation (Equation (2.1)).
4. Calculate the humidity at each node from the diffusion equation (Equation (2.2)).
5. Calculate the phase change rate at each node from the moisture adsorption equation (Equation (2.5)).
6. Calculate the gas volume fraction at each node from the volumetric constraint equation (Equation (2.7)).
7. Repeat steps 2 to 6 until a converged solution field is obtained which satisfies both temperature and vapor density.
8. Repeat steps 2 to 7 for the next time step.

In this chapter, a time step of 0.01s, a grid size of 2.5μm, a normalized convergence criteria of 10^{-8}, and a relaxation factor of 0.001 are used. These values were selected based on sensitivity studies in order to ensure numerical accuracy. With these values, the numerical results satisfy energy and mass balances (a more detailed analysis is given in Appendix C).

2.6 Experiment

An experiment was conducted to verify the numerical model by detecting the onset of frosting on the impermeable plate and permeable membrane described in Table 2.1. The plate/membrane (5 cm × 5 cm) is glued on the test section of the test facility shown in Figure 2.3. The test in this chapter has natural convection conditions for the air above the plate/membrane and forced convection for the liquid desiccant below the plate/membrane (Table 2.2). Cold liquid desiccant ($LiCl$) provided by a thermal bath, flows into the test section to cool the temperature of the plate/membrane aerating a forced convection heat and moisture transfer boundary condition on the bottom of the plate/membrane (Table 2.2). T-Type thermocouples are used to measure the temperature of the liquid desiccant at the inlet and outlet of the test section and also the ambient air temperature. A thermocouple is attached on the upper surface of the membrane/plate in the

center of the test section using thermal paste to measure the surface temperature of the plate/membrane. The humidity ratio of the ambient air is measured during experiments using a capacitance-based RH sensor.

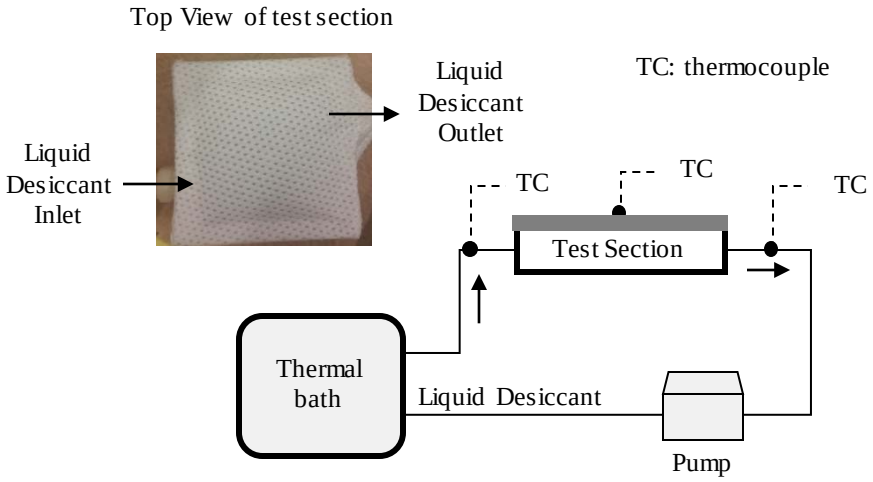

Figure 2.3: Schematic of the experimental facility used to detect the onset of frost on a vapor permeable membrane or impermeable plate.

The thermocouples and RH sensors are calibrated before the experiments with a Hart scientific 9107 Dry Well Calibrator and a Thunder Scientific Model 1200 Mini Humidity Generator respectively, giving systematic uncertainties (B) of ±0.1℃ and ±0.5% RH. The random uncertainties (P) for the thermocouple and RH sensors are equal to ±0.1℃ and ±0.4% RH. The total uncertainty (U) in each thermocouple is calculated to be ±0.14℃ and ±0.64% RH using the following equation (ASME, 2013):

$$U = \sqrt{B^2 + P^2} \tag{2.25}$$

2.7 Results and Discussion

In this section, numerical results showing the temperature and relative humidity profiles in the membrane will be presented to show when and where saturation conditions occur in the membrane for the conditions specified in Table 2.2. In addition, the model will be verified with experimental data and sensitivity studies will be presented to investigate the effect of each parameters on onset of the saturation.

2.7.1 Temperature Profile

In order to find when and where saturation occurs in the membrane, the model must determine the temperature at different locations in the membrane as a function of time. Figure 2.4 presents the temperature as a function of time for different positions within the membrane when the liquid desiccant temperature (T_{LD}) is -10℃ and -15℃ (other boundary conditions are in Table 2.2).

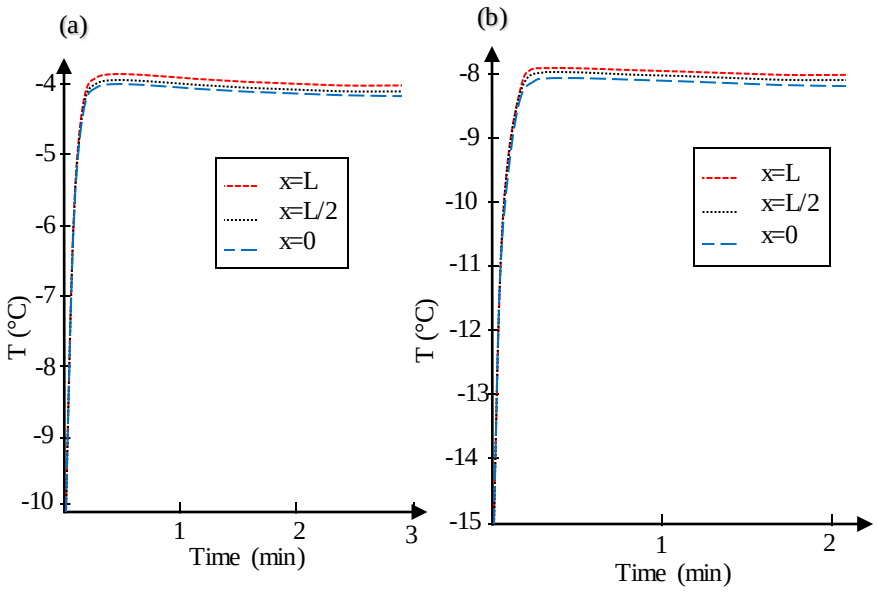

Figure 2.4: Predicted transient temperature on the top ($x = L$) and bottom ($x = 0$) surfaces and the middle ($x = 1/2$) of the membrane as a function of time for (a) $T_{LD} = -10℃$, (b) $T_{LD} = -15℃$.

As can be seen in Figure 2.4, the transient period is very short and the temperatures reach steady state within a few minutes. At the steady state, the temperature difference across the thin membrane (200μm) is small (0.1℃) which means the thermal resistance of the membrane is small compared to the convective heat transfer resistances. Therefore, the steady-state temperature and heat transfer rate through the membrane mainly depend on the temperature of the air and the liquid desiccant, and the convective heat transfer coefficients. Results showed that changing the air relative humidity from $RH_{AIR} = 12\%$ to $RH_{AIR} = 20\%$ does not affect the temperature response and are not presented here.

The temperature profile inside the membrane at different time and steady-state conditions is shown Figure 2.5. As it can be seen, the temperature profile through the membrane is linear at steady-

state (Figure 2.5(b)). It should also be noted that the temperature profile is also quite linear during the transient period (Figure 2.5(a)).

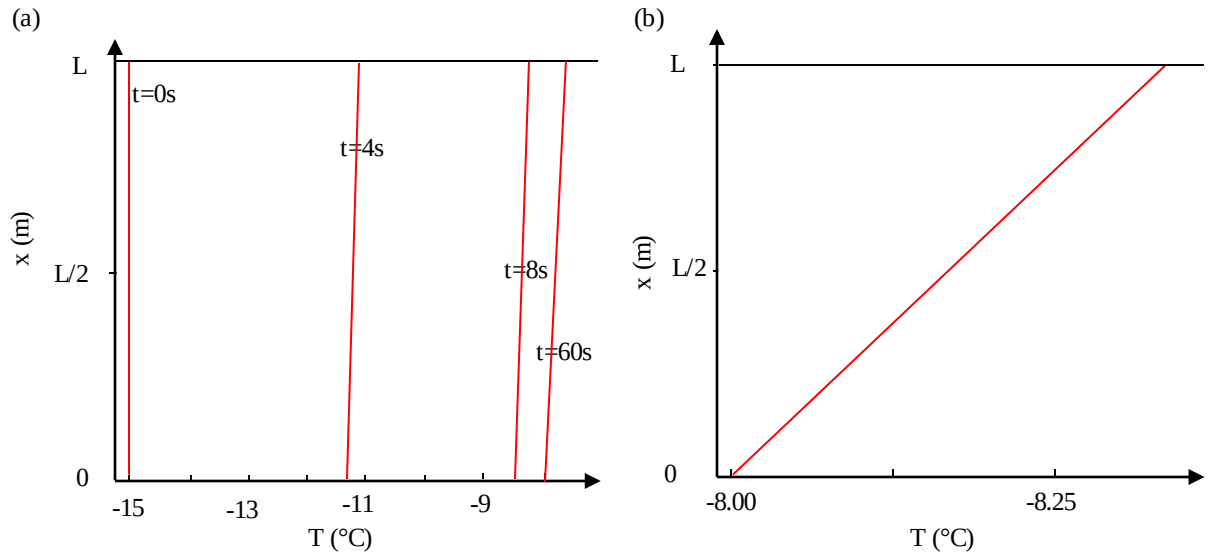

Figure 2.5: Temperature profile within the membrane for $T_{LD} = -15℃$ at (a) different time, (b) steady-state condition.

In order to show that the numerical model calculates temperature accurately, numerical results for the top surface temperature of the membrane at steady-state conditions are verified with experimental results. Figure 2.6 shows the numerical and experimental data for the temperature at the top surface of the membrane $(T_{x=L})$ at steady-state conditions at different liquid desiccant temperatures. The temperature at top surface of the membrane $(T_{x=L})$ decreases as the liquid desiccant temperature (T_{LD}) decreases which is expected. The air relative humidity is constant at $RH_{AIR} = 12\%$ in Figure 2.6. There is good agreement between the numerical and experimental data within the measurement uncertainty. The maximum difference between the numerical and experimental data is 0.8% based on the Equation (2.26).

To further verify the model, the results of the numerical model are compared with the analytical solution (Bergman et al., 2011) for the case of heat transfer only (no moisture transfer). The detailed results are not presented here (see Appendix D), but the average and maximum errors between numerical and analytical data are 0.3% and 1.1% based on Equation (2.26).

$$err = \left| \frac{T_{num} - T_{exp/anl}}{T_{AIR} - T_{LD}} \right| \times 100 \tag{2.26}$$

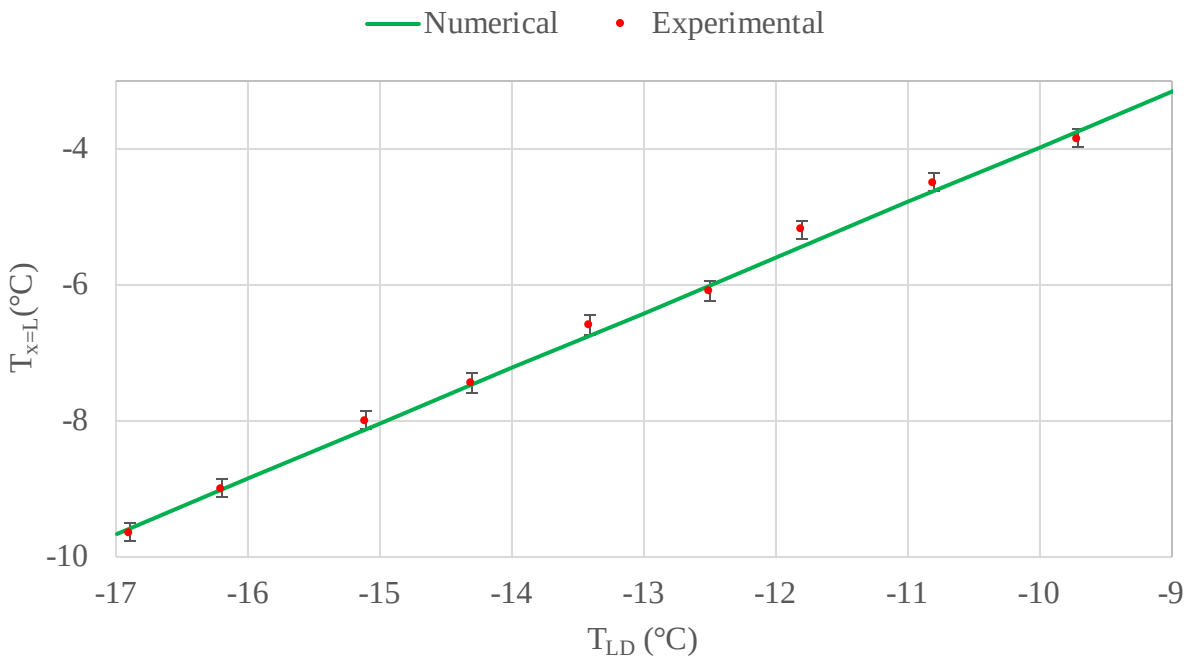

Figure 2.6: Comparison between numerical and experimental temperature of the top surface of the membrane under steady-state conditions when $RH_{AIR} = 12\%$. The error bars indicate the 95% uncertainty bounds in the measured temperature.

2.7.2 Relative Humidity Profile

The relative humidities of the air inside the permeable membrane are presented as function of time in Figure 2.7 for the case of $T_{LD} = -15℃$ and $RH_{AIR} = 12\%$. It should be noted that relative humidity at the top surface of the membrane $(x = L)$ is the highest and is the first location to reach saturation conditions. Thus the top surface is the most critical point of the membrane and should be monitored for saturation conditions. It is reminded that the top surface of the membrane is the warm side of the membrane. As shown in Figure 2.7, the relative humidity at the bottom surface of the membrane is close to the equivalent relative humidity of the liquid desiccant. That is because the mass transfer resistance at the bottom surface of the membrane is much lower than the moisture resistance of the membrane and the mass transfer resistance at the top surface of the membrane.

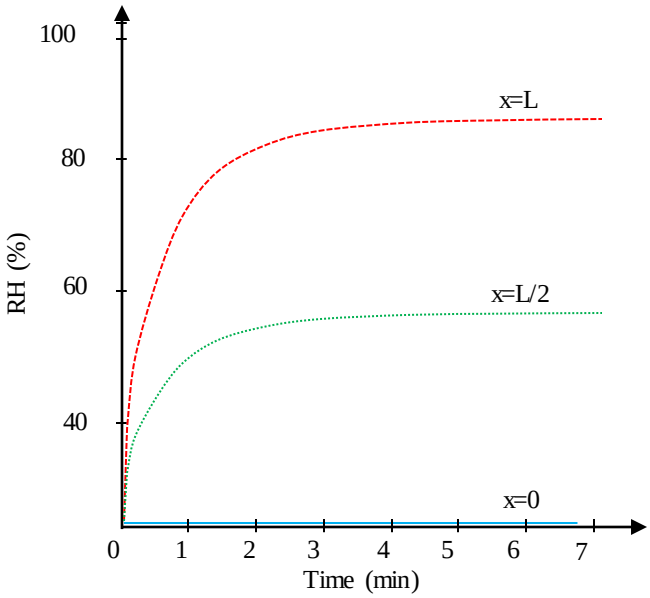

Figure 2.7: Predicted humidity inside the permeable membrane as a function of time when $T_{LD} = -15℃$ and $RH_{AIR} = 12\%$.

The transient relative humidity values of the air at the most critical point in the membrane (i.e., at the top surface) are presented for the permeable and impermeable membrane in Figure 2.8 for the case of $T_{LD} = -15℃$ and $RH_{AIR} = 12\%$ and $RH_{AIR} = 20\%$. Numerical results show that the air within both the permeable and impermeable membrane becomes saturated when $RH_{AIR} = 20\%$. If the humidity of the air above the permeable membrane is 20% RH ($RH_{AIR} = 20\%$), the humidity inside the permeable membrane reaches the saturation line (100%) in about 2 minutes. Therefore, phase change and frosting is expected in this case. However, if $RH_{AIR} = 20\%$ for the impermeable membrane, the humidity inside the impermeable membrane reaches the saturation line (100%) in less than one minute (Figure 2.8(a)). Therefore, moisture transfer through the permeable membrane delays frosting.

Figure 2.8(b) shows that if $RH_{AIR} = 12\%$, the humidity inside the permeable membrane does not reach the saturation line (100%) while the impermeable membrane reaches saturation quite quickly (within about one minute). This means that at these conditions, frost is expected in the impermeable membrane, while no frost is expected in the permeable membrane. Therefore, moisture transfer through the permeable membrane is able to eliminate frosting for these conditions. It should be mentioned that experiments were conducted at $T_{LD} = -15℃$ and $RH_{AIR} =$

12% (Figure 2.8(b)) for the permeable membrane and impermeable plate which will be presented in Section 2.7.3 and experimental results agree with the numerical model.

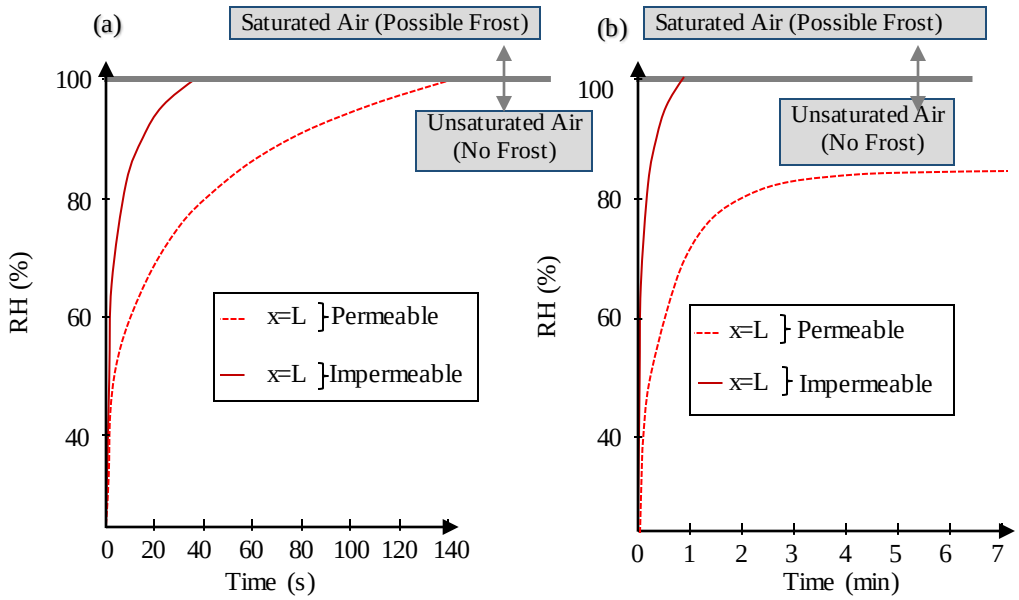

Figure 2.8: Predicted humidity on the top surface of the permeable membrane and impermeable membrane as a function of time for $T_{LD} = -15℃$ and (a) $RH_{AIR} = 20\%$, and (b) $RH_{AIR} = 12\%$.

Figure 2.9 shows the humidity ratio inside the permeable membrane at various times. In Figure 2.9, the humidity ratio has a linear profile with position at steady-state conditions.

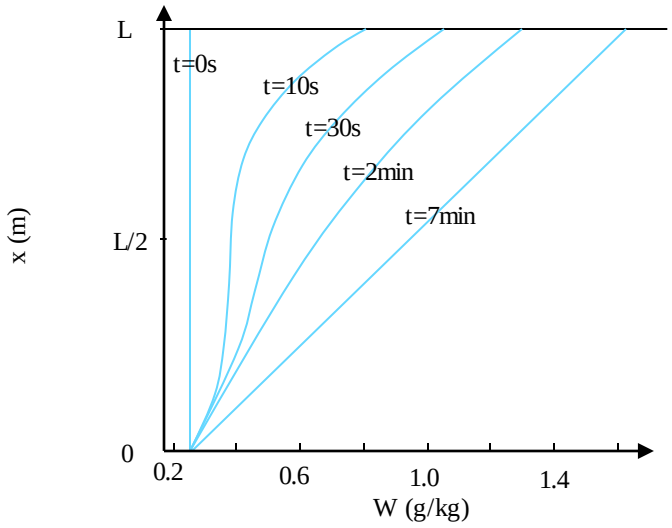

Figure 2.9: Humidity ratio change as a function of time and location within the membrane for $T_{LD} = -15℃$ and $RH_{AIR} = 12\%$.

The numerical model will be verified with experimental data in the next section. Here the numerical model is verified with analytical data (Talukdar et al., 2007) for the case of mass transfer only (no heat transfer). The detailed results are not presented here (see Appendix D), but the average and maximum differences between the numerical and analytical results are 0.4% and 1.3% based on the following equation:

$$err = \left| \frac{\rho_{num} - \rho_{anl}}{\rho_{AIR} - \rho_{LD}} \right| \times 100 \tag{2.27}$$

Figures 2.5 and 2.9 show that the temperature and humidity profiles inside the membrane are linear at steady state. Therefore, it may be possible to develop an analytical model based on the thermal and mass resistance that is able to accurately predict the temperature and relative humidity at the top and bottom surfaces of the membrane under steady-state conditions. This will be pursued in Chapter 3 of this thesis.

2.7.3 Detection of Frost at Steady-state Conditions

This section will present the effect of T_{LD} and RH_{AIR} on the relative humidity of the air at the top surface of the membrane/plate. In each case, pictures from experimental will be presented to verify the predictions of the numerical model.

2.7.3.1 Effect of Liquid Desiccant Temperature

Figures 2.10 and 2.11 present numerical results for the steady-state relative humidity at the top surface of the membrane/plate ($RH_{x=L}$) as a function of liquid desiccant temperature for the permeable membrane and impermeable plate, respectively. Figures 2.10 and 2.11 also contain pictures of the membrane/plate for experiments with and without frosting. The air relative humidity is 12% in Figure 2.10 and 2.11. Figure 2.10 shows that the models predict that $RH_{x=L}$ will increase from 78% RH to 100% RH as T_{LD} decreases from -14℃ to -17℃ for the permeable membrane. Thus saturation and frosting is expected for $T_{LD} \leq -17$℃. The picture from the experiment confirm the frost limit of $T_{LD} = -17$℃ predicted by the model as the photograph from the test with $T_{LD} = -16$℃ shows no frost while the photograph at $T_{LD} = -17$℃ shows a distinct frost layer on the membrane. Similar results are seen in Figure 2.11 for the impermeable plate,

except frost is predicted and confirmed for $T_{LD} \leq -15°C$. Both the numerical and experimental data show that moisture transfer through the membrane delays frosting.

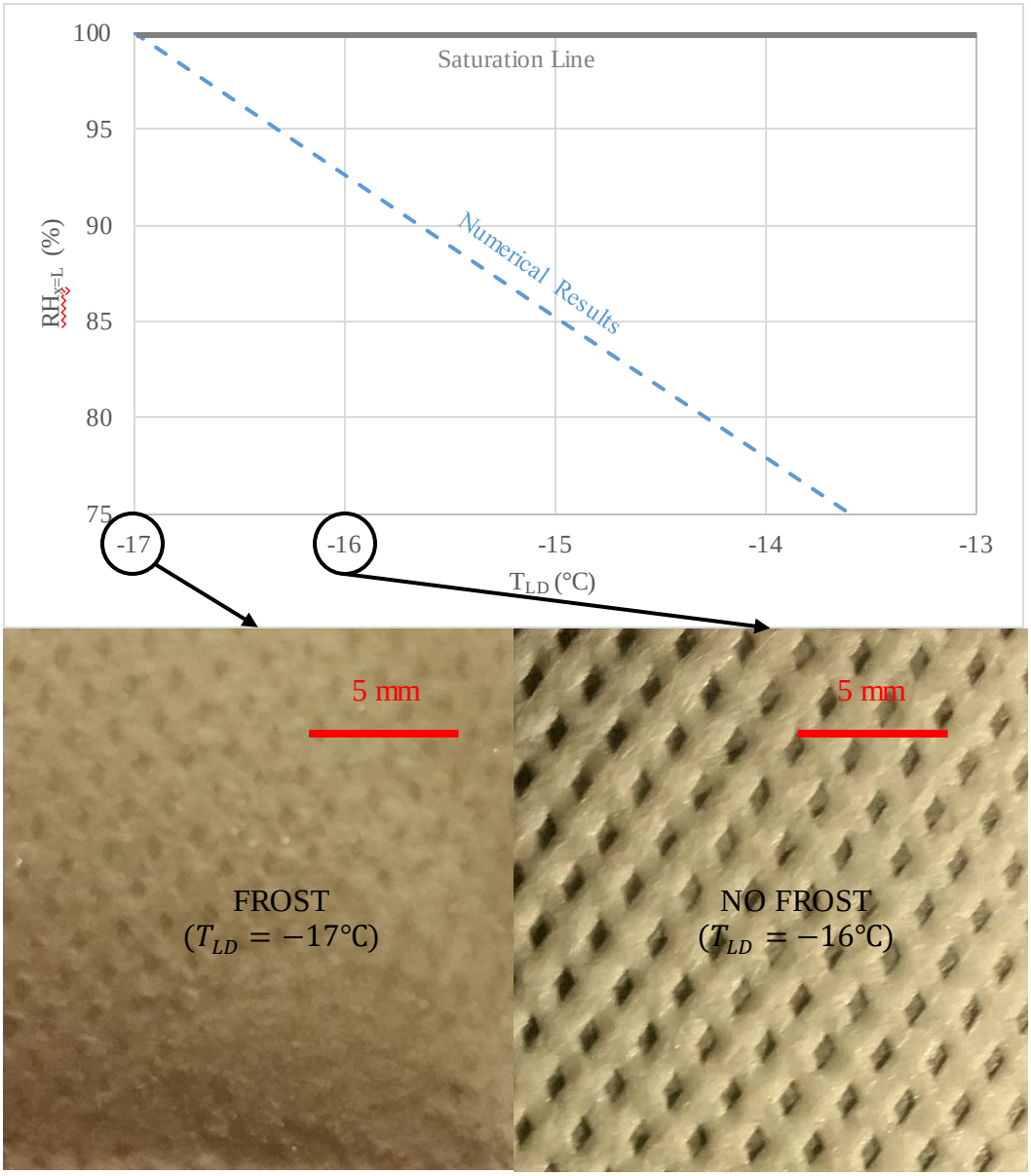

Figure 2.10: Simulated relative humidity on the top surface of the permeable membrane as a function of the liquid desiccant temperature at steady state when $RH_{AIR} = 12\%$. Pictures of the top surface of the permeable membrane are presented for $T_{LD} = -17°C$ and $T_{LD} = -16°C$ (There is a white layer of frost on the permeable membrane when $T_{LD} = -17°C$).

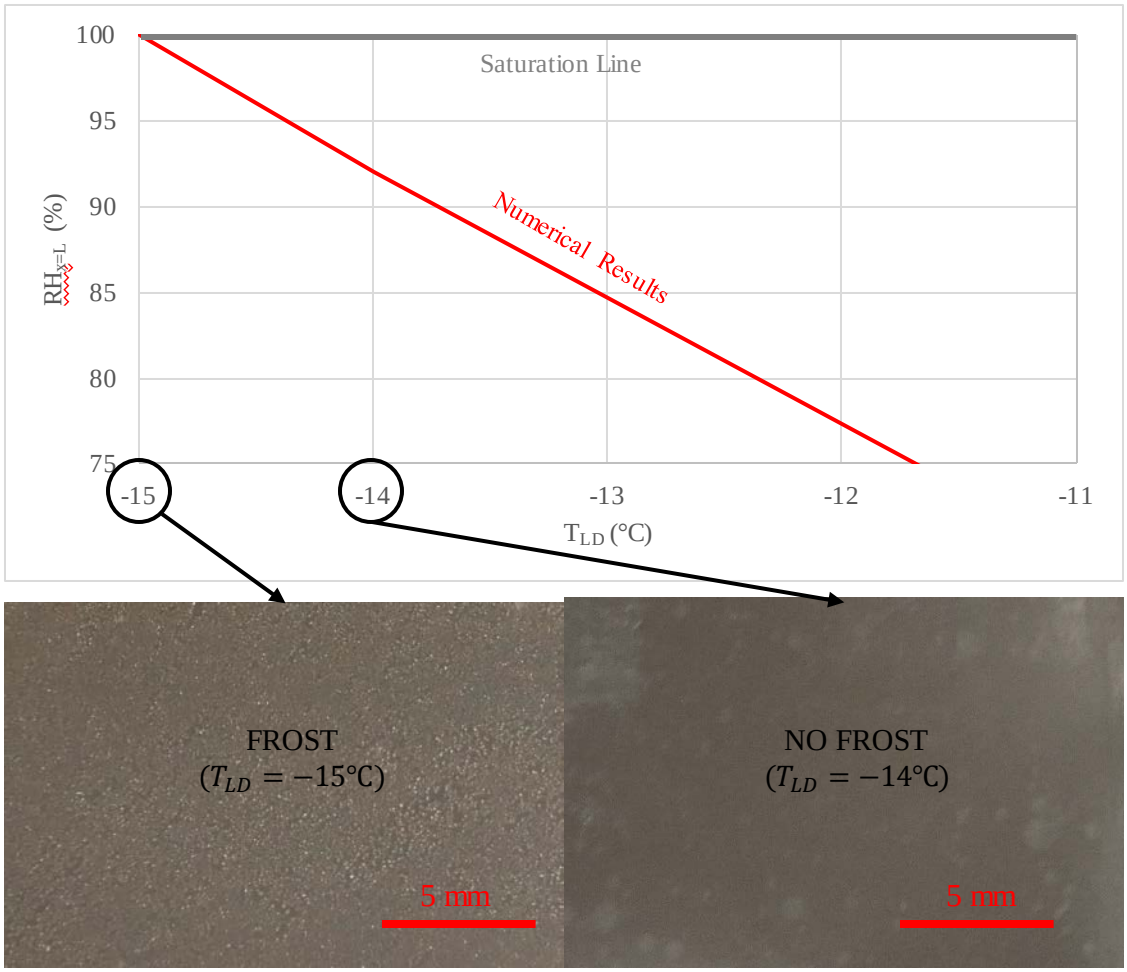

Figure 2.11: Simulated relative humidity on the top surface of the impermeable plate as a function of the liquid desiccant temperature at steady state when $RH_{AIR} = 12\%$. Pictures of the top surface of the impermeable plate are presented for $T_{LD} = -15$°C and $T_{LD} = -14$°C (The white spots in the images are frost crystals and are present for $T_{LD} = -15$°C but are absent for $T_{LD} = -14$°C).

2.7.3.2 Effect of Air Relative Humidity

If air relative humidity increases, there is a greater risk of frosting in the membrane. Figure 2.12 presents the numerical results for the steady-state values of the relative humidity at the top surface of the membrane ($RH_{x=L}$) as a function of the air relative humidity (RH_{AIR}) for the permeable membrane and impermeable plate. Once again, the top surface of the membrane is presented because it is the most critical location and reaches saturation conditions first (Figure 2.8). The liquid desiccant temperature is -15°C in Figure 2.12.

As RH_{AIR} increases, $RH_{x=L}$ increases for both the membrane and plate. Saturation conditions exist (numerical model) when $RH_{AIR} \geq 11\%$ for the impermeable plate and for $RH_{AIR} \geq 16\%$ for the permeable membrane. The model is verified by pictures from experiments with $T_{LD} = -15℃$ and $RH_{AIR} = 12\%$. The pictures in Figure 2.12 show that there is frost on the impermeable plate at $RH_{AIR} = 12\%$ but no frost on the permeable membrane at $RH_{AIR} = 12\%$ (Figure 2.12). Comparing the results for the permeable membrane and impermeable plate shows that moisture transfer through the membrane delays frosting. It should be mentioned that numerical results for the impermeable membrane are the same as the impermeable plate.

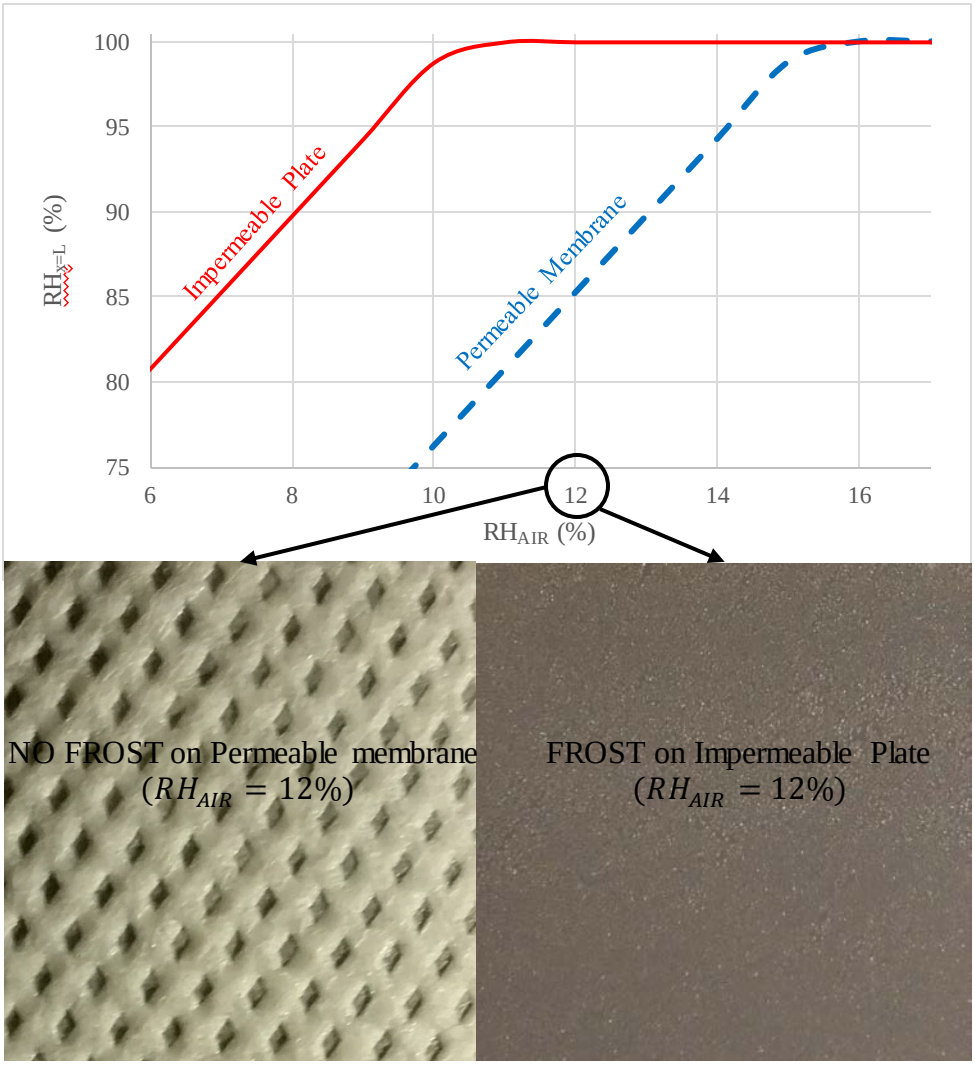

Figure 2.12: Simulated relative humidity on the top surface of the membrane as a function of air relative humidity for steady-state conditions when $T_{LD} = -15℃$. Pictures of the top surface of the membrane are presented for $T_{LD} = -15℃$ and $RH_{AIR} = 12\%$ (The white points on the impermeable plate are frost crystals meanwhile there is no frost on the permeable membrane).

2.7.4 Sensitivity Studies

Sensitivity studies can show how different values of each of the properties impact the time at which saturation (frosting) occurs (i.e., the saturation time) when all other properties are constant. Saturation time is defined as the time when relative humidity inside the membrane reaches saturation conditions. Figure 2.13 shows the impact of different membrane properties on the saturation time when liquid desiccant temperature is -15℃ and air relative humidity is 20%.

With $T_{LD} = -15℃$ and $RH_{AIR} = 20\%$, the saturation time is two minutes for the base membrane properties. As shown in Figure 2.13, changing the density, moisture content, thickness, and diffusion coefficient of the membrane have a noticeable effect on saturation time. These parameters affect moisture transfer and thus they influence the saturation time. On the other hand, the heat capacity (c_p) and thermal conductivity (k) have a negligible effect on saturation time because heat capacity and thermal conductivity do not affect moisture transfer. These results confirm the hypothesis that moisture transfer affects saturation. It should be noted that changing heat capacity, density, moisture content, and the diffusion coefficient do not change surface temperature (Figure 2.13(a)), meanwhile, changes in thermal conductivity, and the thickness of the membrane change surface temperature (Figure 2.13(b)). As shown in Figure 2.13, changing the membrane properties can delay the onset of saturation which would also delay the onset of frosting. However, the maximum delay is less than five minutes in all the cases tested.

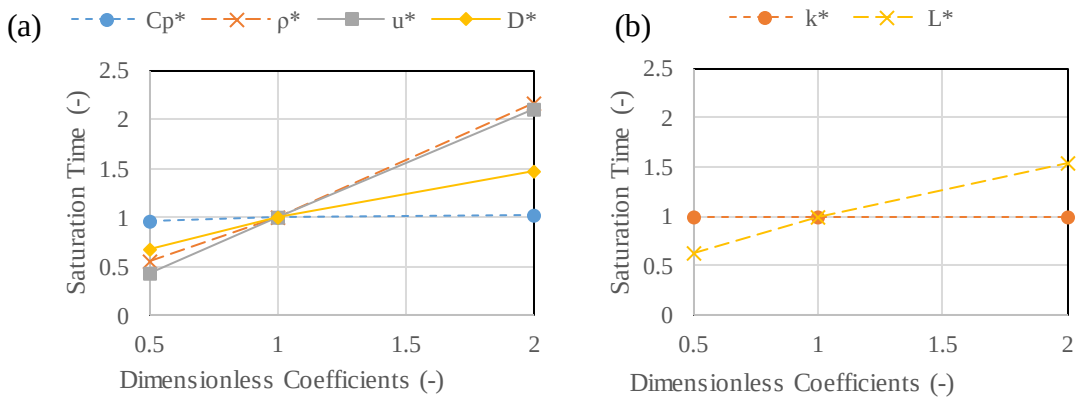

Figure 2.13: Impact of dimensionless coefficients on dimensionless saturation time when $T_{LD} = -15℃$ and $RH_{AIR} = 20\%$ for different dimensionless, (a) heat capacity, density, moisture content, and diffusion coefficient (b) thermal conductivity, and thickness of the membrane.

2.8 Conclusion

In this chapter, a numerical model that predicts the onset of saturation conditions in permeable membranes has been developed and verified with experimental and analytical data. Saturation conditions are required for frosting to occur. Numerical and experimental data show that moisture transfer through the membrane can delay frost formation and even prevent frost formation for some conditions. Therefore, the results in this chapter confirm that it is feasible to achieve a frost-free exchanger with a vapor permeable membrane. Numerical results show that changing the moisture properties of the membrane by a factor of two can delay the onset of saturation, but for less than five minutes. Therefore, in practice, delaying saturation is not as promising as avoiding saturation conditions to achieve a frost-free exchanger with a vapor permeable membrane. Based on these findings, it is important to investigate the effects of different parameters which influence frost formation at the steady-state condition in order to prevent frosting. The results in this chapter also show that the temperature and relative humidity at steady-state conditions can possibly be calculated using an analytical model based on thermal and mass resistance. An analytical model will be the focus of the next chapter of this thesis.

CHAPTER 3

ANALYTICAL MODEL

3.1 Overview of Chapter 3

In this chapter, a simplified, analytical solution to the transient numerical model of Chapter 2 is used to study the onset of saturation at steady state. Steady state is considered in this chapter because Chapter 2 showed that membrane properties have only a small effect on the time at which saturation occurs. Therefore, in order to achieve frost-free exchangers, saturation should be avoided at steady state. This chapter studies a range of membrane properties and operating conditions which influence onset of saturation to prevent frosting within a membrane.

This chapter has been submitted to the International Journal of Heat and Mass Transfer with three contributing authors. Pooya Navid (MSc student) performed the study and wrote the manuscript. Shirin Niroomand (PhD student) reviewed the manuscript, wrote Section 3.6, and generated the experimental data. Carey J. Simonson (MSc supervisor) supervised the study and reviewed the manuscript.

Analytical model for predicting frosting limit in membranes

Pooya Navid, Shirin Niroomand, Carey J. Simonson

3.2 Abstract

Membrane energy exchangers have been used in the HVAC industry recently in order to reduce energy consumption and reduce the risk of frost formation. In this chapter, frosting in membranes is studied with an analytical model based on thermal and mass resistances to determine the temperature and relative humidity at the surface of a membrane at steady state. The model is verified with experimental and numerical data. The main goal of this chapter is to investigate the effects of design and operating parameters on the onset of saturation in order to prevent or delay frosting in a membrane. The maximum cold temperature which leads to frost formation on a surface at a specific air relative humidity is defined as the frosting limit. The frosting limit for a membrane is presented for different temperature and humidity conditions. A new parameter, allowable dew point depression of the surface (ΔDP), is defined as the difference between the dew point temperature of the air stream and the temperature at the top surface of the membrane. A sensitivity study of ΔDP demonstrates that the water vapor permeability of the membrane, heat transfer coefficient, and thickness of the membrane impact the frosting limit. The main conclusion is that increasing the moisture transfer rate through the membrane decreases the frosting limit.

3.3 Introduction

Frosting is a common phenomenon in energy systems that operate under the freezing point. Frosting occurs when the surface temperature is below the dew point and also the freezing point of water. Frost is a porous media consisting of ice crystals and air. Therefore, the thermal resistance of frost is considerable. Frosting occurs in many industries like the food industry (Tassou et al., 2001), oil industry (Mike, 2014), aviation industry (Cao et al., 2015), and the HVAC (Heating, Ventilation and Air Conditioning) industry (Rafati Nasr et al., 2014). The frost layer acts like a thermal insulator between the two fluids in heat exchangers and decreases the air flow area which leads to higher pressure drop and fan energy consumption. Thus, frosting decreases the system performance (Amer and Wang, 2017). Different defrosting techniques have been suggested to overcome the frosting problem (Rafati Nasr et al., 2014).

Membranes have been used widely in industries such as food and beverage (Cassano and Conidi, 2017; Bhattacharjee et al., 2017), water treatment (Alzahrani and Mohammad, 2014), pharmaceutical (Yu et al. 2011, Sirkar 2000), gas separation (Hamm et al. 2017), and HVAC systems (Abdel-Salam et al., 2014; Rafati Nasr et al., 2015). A flat-plate liquid-to-air membrane energy exchanger (LAMEE) is one membrane exchanger in the HVAC industry. A LAMEE allows heat and moisture transfer between an air stream and a liquid desiccant through a permeable membrane in order to increase the sensible and latent efficiency of the energy systems (Abdel-Salam et al., 2014).

Studies have shown that moisture transfer can decrease frosting in energy exchangers like energy wheels (Shang et al., 2005; Mahmood and Simonson, 2012). Furthermore, studies have shown that the moisture transfer through a membrane can prevent or delay frost formation (Figure 2.8 and 2.11; Rafati Nasr et al., 2015). Also, the performance of membrane energy exchangers under frosting operating conditions is better than the performance of heat exchangers (Alonso et al., 2017).

The main objective of this chapter is to investigate the effects of design and operating parameters on the onset of saturation in order to prevent or delay frosting. The concept is to dry and cool the air in contact with the membrane to prevent saturation conditions and thereby eliminate phase change (frosting).

3.4 Physical Model

A schematic of the problem of heat and moisture transfer through a permeable membrane separating two fluids in a LAMEE is presented in Figure 2.1. Table 2.1 shows the properties of the selected permeable membrane (Propore™) for this study. As depicted in Figure 2.1, warm and humid air passes over the top of the membrane and cold liquid desiccant passes under the bottom of the membrane. It is assumed that the length and the width of the membrane are much greater than the thickness. Also, the sides of the membrane are assumed impermeable and adiabatic. Therefore, the heat and moisture transfer are one-dimensional.

3.5 Analytical Model

It has been shown in Chapter 2 that the temperature and humidity profiles inside the membrane are linear at steady-state conditions. Therefore, an analytical model based on thermal and mass resistance can be implemented. The analytical model, based on the thermal and moisture resistance presented in Figure 3.1, is presented in Equation (3.1) and (3.2). All symbols are defined in the Nomenclature section. The results in Chapter 2 (Figure 2.8) show that saturation (RH=100%) usually occurs on the warm and humid side of the membrane (i.e., at $x = L$).

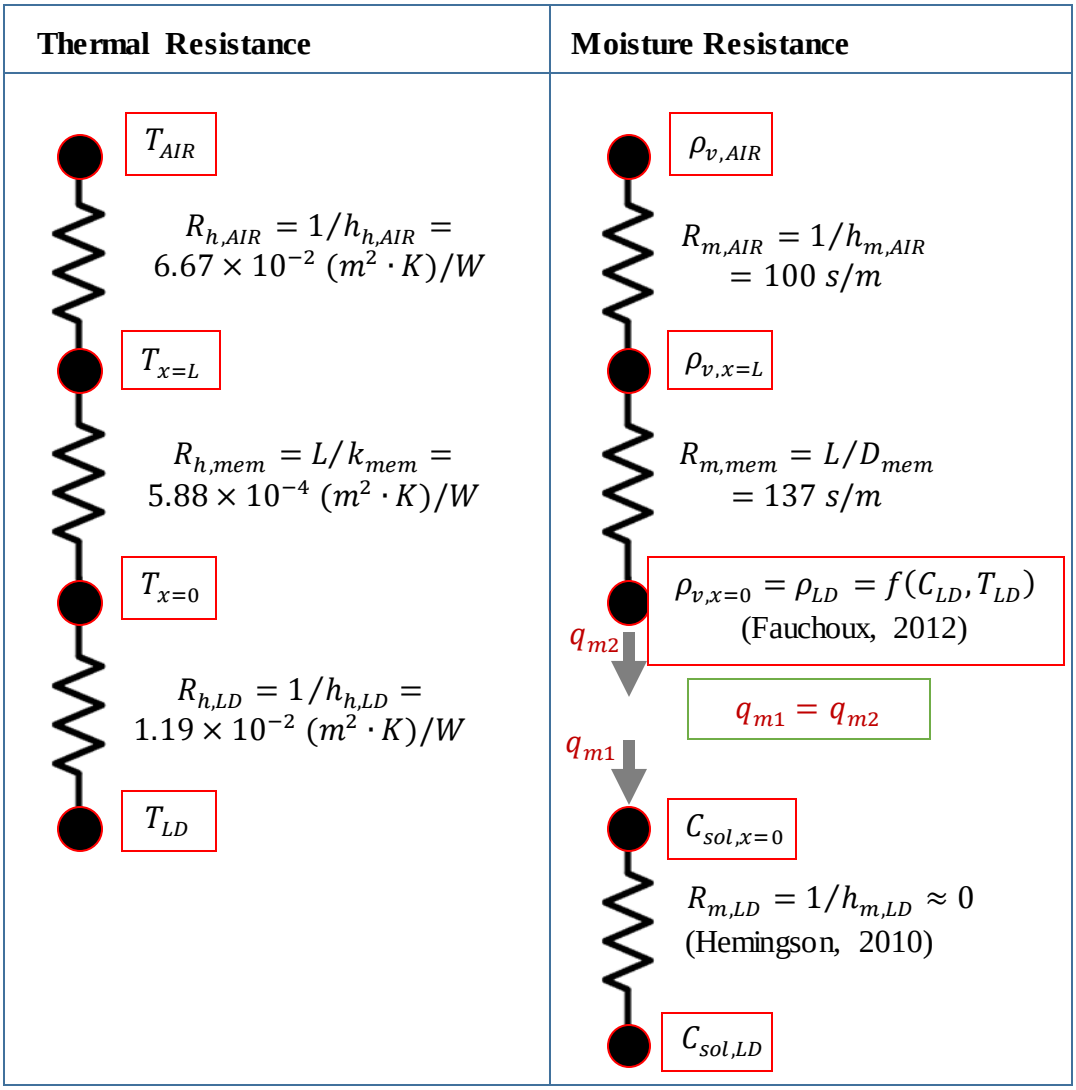

Figure 3.1: Thermal resistance and moisture resistance for a membrane.

$$q_h = \frac{T_{AIR} - T_{x=L}}{R_{h,AIR}} = \frac{T_{x=L} - T_{x=0}}{R_{h,mem}} = \frac{T_{x=0} - T_{LD}}{R_{h,LD}} \tag{3.1}$$

$$q_{m2} = \frac{\rho_{v,AIR} - \rho_{v,x=L}}{R_{m,AIR}} = \frac{\rho_{v,x=L} - \rho_{v,x=0}}{R_{m,mem}} \tag{3.2}$$

Equation (3.1) and (3.2) can be rearranged to give the temperature and water vapor density at top and bottom surfaces of the membrane:

$$\begin{aligned} T_{x=0} &= \frac{T_{x=L}\left(R_{h,mem} + R_{h,AIR}\right) - R_{h,mem}T_{AIR}}{R_{h,AIR}} \\ &= \frac{h_{h,AIR}LT_{AIR} + \left(k_{mem} + h_{h,AIR}L\right)\left(h_{h,LD}L\right)T_{LD}}{\left(\left(k_{mem} + h_{h,AIR}L\right)\left(k_{mem} + h_{h,LD}L\right) - k_{mem}\right)} \end{aligned} \tag{3.3}$$

$$T_{x=L} = \frac{\left(R_{h,mem} + R_{h,LD}\right)R_{h,mem}T_{AIR} + R_{h,mem}R_{h,AIR}T_{LD}}{\left(R_{h,mem} + R_{h,LD}\right)\left(R_{h,mem} + R_{h,AIR}\right) - R_{h,LD}R_{h,AIR}} = \frac{LT_{AIR} - k_{mem}T_{x=0}}{L + \frac{k_{mem}}{h_{h,AIR}}} \tag{3.4}$$

$$\rho_{v,x=L} = \frac{R_{m,AIR}\rho_{v,x=0} + R_{m.mem}\rho_{v,AIR}}{R_{m,AIR} + R_{m,mem}} \tag{3.5}$$

The water vapor density and temperature are converted to relative humidity to determine if the air is saturated by using the following thermodynamic relations:

$$p_v = R_v\rho_v T \tag{3.6}$$

$$RH = \frac{p_v}{p_{sat}} \tag{3.7}$$

where p_{sat} is a function of temperature (ASHRAE, 2013).

The algorithm used to calculate the temperature and relative humidity can be summarized as follows:

1. Input physical data, including physical properties (thickness, thermal conductivity, diffusion coefficient of the selected membrane) and operating conditions (temperature, relative humidity, heat and mass transfer coefficient at both sides of the membrane).
2. Calculate the temperature at top and bottom of the membrane from the thermal resistance (Equation (3.3) and (3.4)).
3. Calculate the vapor density at top of the membrane from the moisture resistance (Equation (3.5)).
4. Calculate the relative humidity at top and bottom of the membrane from the moisture resistance (Equation (3.6) and (3.7)).

The design (Table 2.1) and operating conditions in (Table 3.1) that will be studied are based on the experimental tests conducted on the Propore™ membrane. The experiments are described in Section 3.6. Both convection and radiation heat transfer are considered on the top and bottom of the membrane. In order to find mass transfer coefficient, an analogy between the convective heat and mass transfer coefficients is used.

Table 3.1: Operating conditions.

Parameters	Unit	Value
Liquid Desiccant		
Temperature (T_{LD})	℃	-3 to -14
Equivalent relative humidity ($Eqv.RH_{LD}$)	%	50
Concentration (C_{LD})	%	26
Heat transfer coefficient ($h_{h,LD}$)	W/(m^2·K)	84
Mass transfer coefficient ($h_{m,LD}$)	m/s	∞ (Hemingson, 2010)
Air		
Temperature (T_{AIR})	℃	22
Relative humidity(RH_{AIR})	%	10 to 40
Heat transfer coefficient ($h_{h,AIR}$)	W/(m^2·K)	15
Mass transfer coefficient ($h_{m,AIR}$)	m/s	0.01

For sensitivity studies, dimensionless properties, D^*, $h^*_{h,AIR}$, $h^*_{h,LD}$, L^*, k^*, and C^* are defined relative to the base case properties in Table 2.1 and Table 3.1 and Equation (3.8).

$$\alpha^* = \frac{\varphi_{new}}{\varphi_{base}} \tag{3.8}$$

where, α^* is a general dimensionless property (D^*, $h^*_{h,AIR}$, $h^*_{h,LD}$, L^*, k^*, and C^*), φ_{new} is the value of new property for the sensitivity study and φ_{base} is the value of property in Table 2.1 and Table 3.1.

A new parameter, allowable dew point depression of the surface (ΔDP), is defined as the difference between the dew point temperature of the air stream and the temperature at the top surface of the membrane (Equation (3.9)). For an impermeable plate frost forms when $\Delta DP \leq 0$ (i.e., $DP_{AIR} \geq T_{x=L}$). For a permeable membrane ΔDP may be greater than zero, which means that frosting (saturation) may not occur even when the dew point temperature of the air is greater than the membrane surface temperature. The higher the value of ΔDP, the more the membrane is able to avoid frosting.

$$\Delta DP = DP_{AIR} - T_{x=L} \tag{3.9}$$

3.6 Experiment

A test facility was designed to study the effect of moisture transfer on frosting, under forced convection conditions, as seen in Figure 3.2(a). The test facility was designed to create a cold surface with warm humid air passing over top of the surface. The test facility consists of a test section, a cold liquid loop and an air channel. The cold liquid loop consists of a pump, a thermal bath, which cools the liquid to the desired temperature, and a storage container.

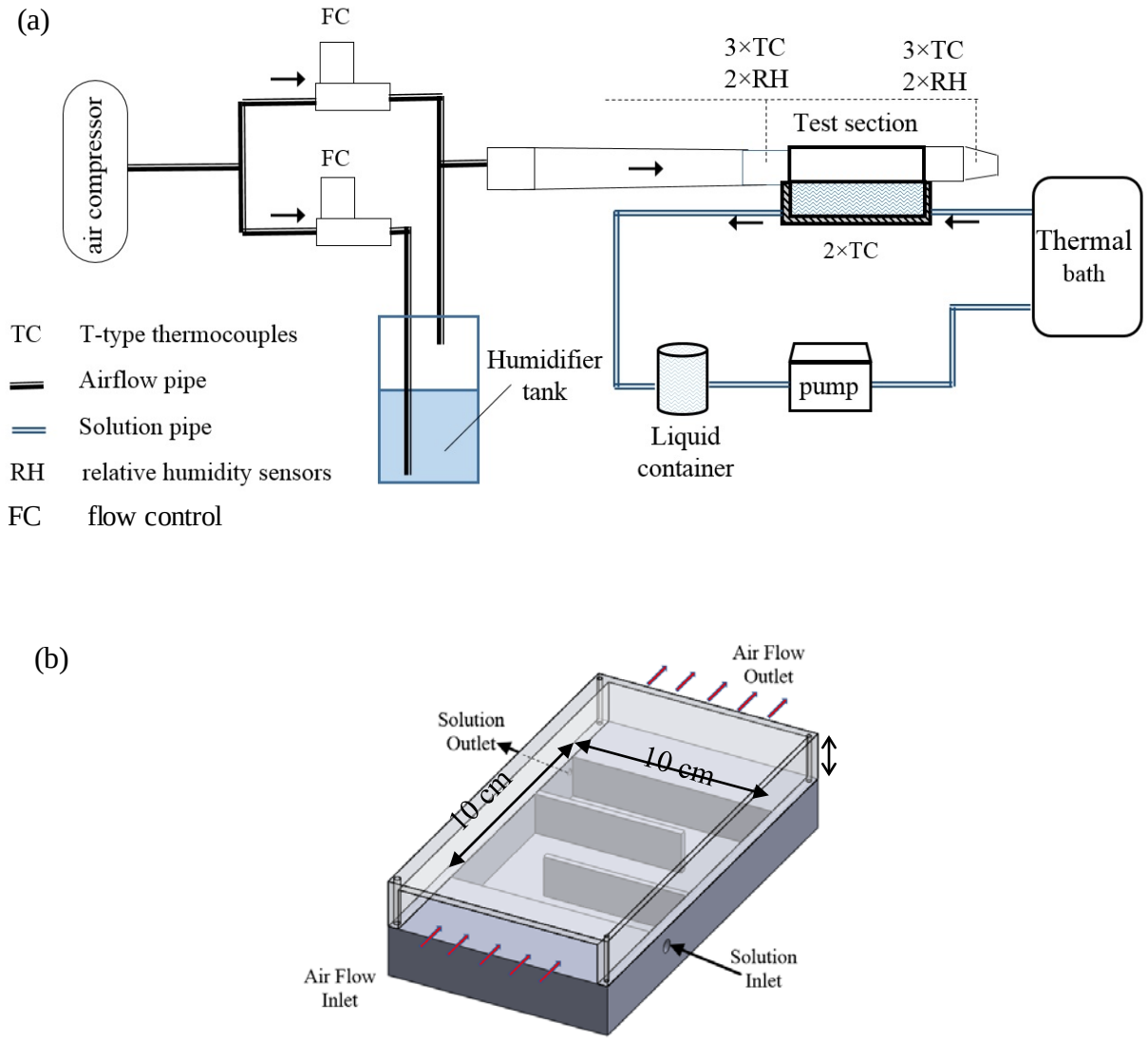

Figure 3.2: Schematic of the test setup (a) test facility (b) test section.

On the air side, dry air at room temperature is supplied to the test facility from a compressor. Prior to the test section, the air stream is divided into two; one air stream passes through a well-sealed tank of water (humidifier tank) to create humid air, and the other air stream bypasses the tank to maintain dry air. The two air streams are then mixed to create one air flow. The volume flow rate of both air streams were set and controlled using two Mass-Flow Controllers with a maximum flow rate of 200 L/min. Depending on the mass flow rate of humid air and dry air, the humidity ratio of the mixed air was changed. The total air flow rate is the summation of both mass flow

rates. The air channel was designed so that the air flow would be fully developed prior to entering the test section.

The temperature of the air is measured at three points across the width of the air channel both upstream and downstream of the test section, using T-type thermocouples. The relative humidity of the air is measured at two points across the width of the air channel at the same locations using Honeywell HIH humidity sensors. Only two relative humidity measurements were taken at each location due to the size of the relative humidity sensors being slightly larger than the thermocouples. The temperature and relative humidity measurements were taken across the width of the air channel and the average values will be reported as inlet and outlet conditions. The thermocouples were calibrated with a Hart scientific 9107 Dry Well Calibrator. The systematic uncertainty in thermocouples is ±0.1℃. The random uncertainties for the thermocouples ranged from ±0.02℃ to ±0.06℃. The humidity sensors were calibrated with a Thunder Scientific Model 1200 Mini Humidity Generator. The sensors had a systematic uncertainty of ±0.5% RH, and a random uncertainty between ±0.3% RH and ±0.4% RH. The uncertainty of each mass flow controller is about 1% of the maximum flow rate. The maximum random uncertainty in the volume flow rates was 0.007 L/min. The total uncertainty in each thermocouple and RH sensor is calculated using root-sum-squared of the systematic and random uncertainties Equation (2.25) (ASME, 2013)

A schematic of the test section, with dimensions, is shown in Figure 3.2(b). The test section allows the cold fluid to flow evenly through the test section. The top section is made of clear acrylic to allow for visualization of the cold surface during testing.

The cold liquid used for this research is a salt solution consisting of water and Lithium Chloride ($LiCl$). A salt solution is used, as it is a liquid desiccant, which can absorb water vapor from the airflow.

Frosting tests were performed on two different surfaces, a permeable membrane and an impermeable plate. The permeable membrane used in this research was Propore™. The plate is an impermeable surface with approximately the same thermodynamic properties as the permeable membrane. As moisture cannot transfer through the plate, comparison of the frost limits for the plate and for the membrane will show the effect of moisture transfer rate on the frost formation.

The temperature of the surface on the air side was measured during each test. One T-type thermocouple was attached to the surface using thermal paste in the center of the test cell. It was seen that for a fixed liquid temperature, the surface temperature for both membrane and plate were very close to each other (with ±0.2℃).

3.7 Results and discussion

In this section, the frosting limits for different design and operating parameters (Table 3.2) are presented. In addition, the model will be verified with experimental data and the location of saturation conditions will be investigated.

Table 3.2: Design and operating parameters.

Design parameters	**Operating parameters**
vapor diffusion coefficient of the membrane(D_{mem})	liquid desiccant concentration (C_{LD})
thickness of the membrane(L)	heat and mass transfer coefficient of air side ($h_{h,AIR}$ and $h_{m,AIR}$)
thermal conductivity of the membrane (k_{mem})	heat and mass transfer coefficient of liquid desiccant side ($h_{h,LD}$ and $h_{m,LD}$)
density of the membrane(ρ_{mem})	liquid desiccant temperature (T_{LD})
heat capacity of the membrane ($c_{p,mem}$)	air relative humidity(RH_{AIR})

3.7.1 Model verification

As mentioned previously, the maximum liquid desiccant temperature (T_{LD}) which leads to frost formation on a membrane at a specific air relative humidity (RH_{AIR}) is defined as the frosting limit. The analytical model is solved for different T_{LD} and RH_{AIR} to determine the conditions where RH=100% at $x = L$, which is the point where saturation first begins as shown in Chapter 2 (Figure 2.7). The combination of T_{LD} and RH_{AIR} that leads to $RH_{x=L}$=100% is defined as the frosting limit. The frosting limit calculated with the analytical model is presented in Figure 3.3 for the impermeable plate and in Figure 3.4 for the permeable membrane. Numerical results at steady state and experimental data are also included to verify the analytical model. In Figures 3.3 and 3.4, filled

circles indicate that frost was detected experimentally and x symbols indicate that frost did not occur experimentally. Analytical results show good agreement with the numerical and experimental data for both the impermeable plate and the permeable membrane.

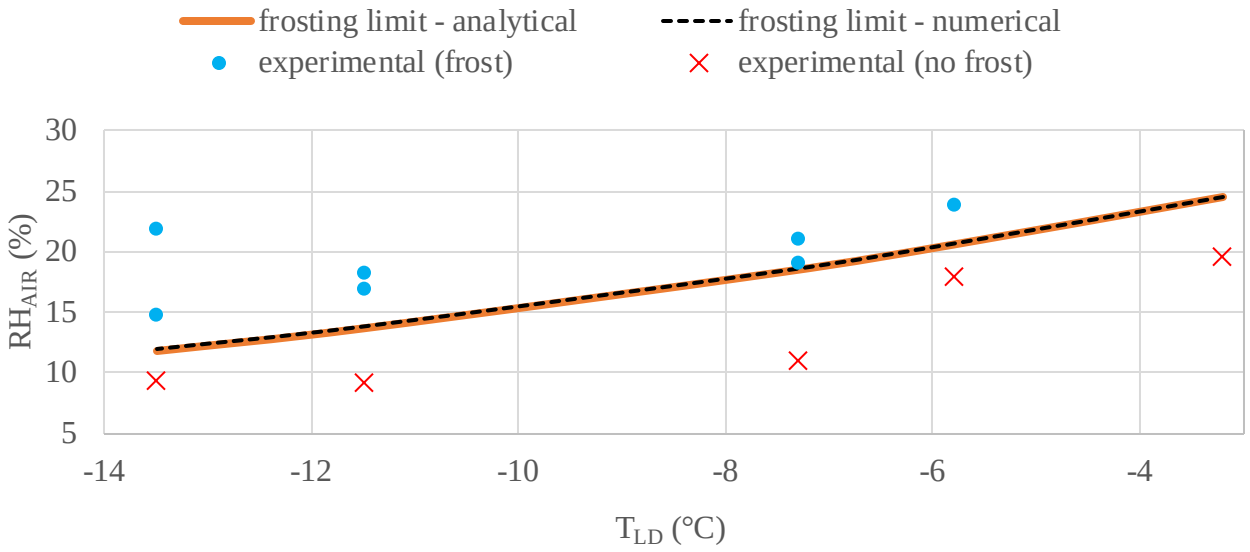

Figure 3.3: Analytical frosting limit compared to numerical and experimental data with and without frosting for the impermeable plate.

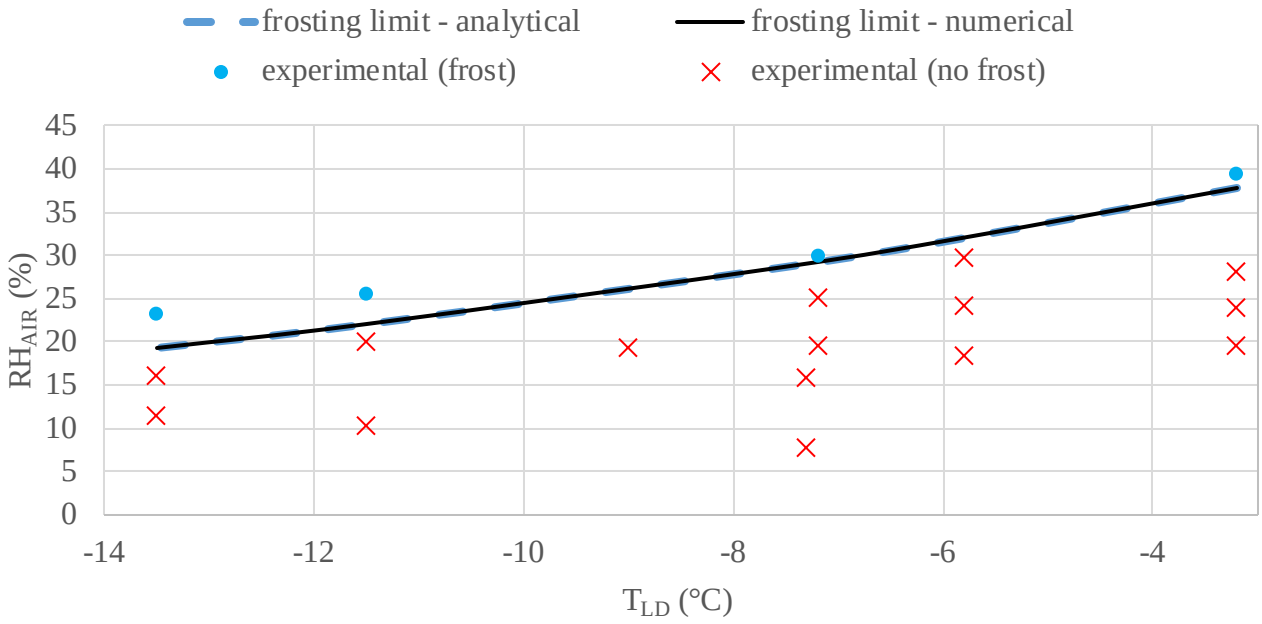

Figure 3.4: Analytical frosting limit compared to numerical and experimental data with and without frosting for the permeable membrane.

As mentioned previously, the analytical model is one-dimensional. However, the experimental boundary conditions are not uniform as the fluid conditions are different at the inlet and outlet of the test section. Figure 3.5 presents a sensitivity study of frosting limit to the measured inlet, outlet, and average conditions in the experiment for boundary conditions in Table 3.1. In the experiment, the inlet air temperature decreases between 2°C and 5°C depending on liquid desiccant temperature. The inlet air relative humidity decreases between 2% RH and 4% RH. The liquid desiccant temperature is constant due to higher thermal capacity of liquid desiccant compared to the air. The change in liquid desiccant concentration before and after the experiment is negligible. As illustrated, selecting the inlet or outlet conditions changes the RH_{AIR} that leads to frosting by about ±3% compared to using the average conditions.

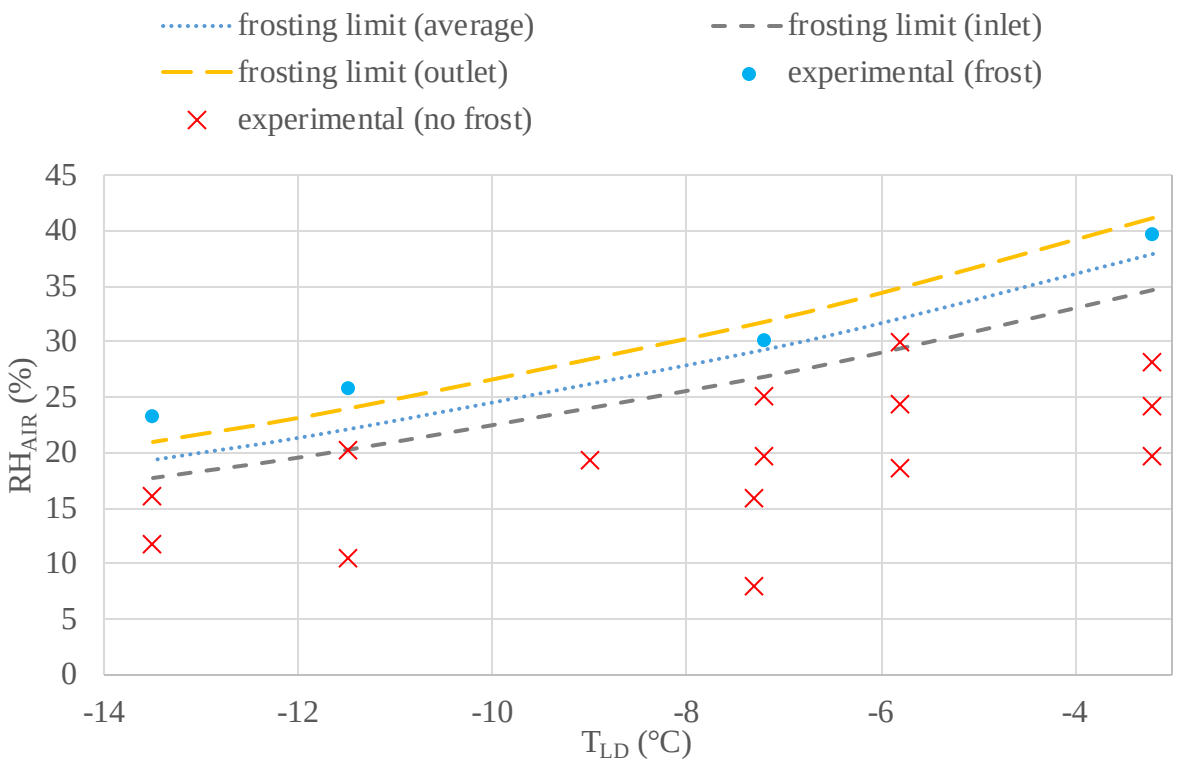

Figure 3.5: Sensitivity of analytical results to inlet, outlet, and average conditions for permeable membrane.

The temperature of the top surface of the membrane ($T_{x=L}$) depends on liquid desiccant temperature (T_{LD}) and membrane properties like thickness and thermal conductivity. Figure 3.6 presents the relationship between the top surface temperature and liquid desiccant temperature at

steady state when the air relative humidity (RH_{AIR}) is 20% (other boundary conditions are in Table 3.1).

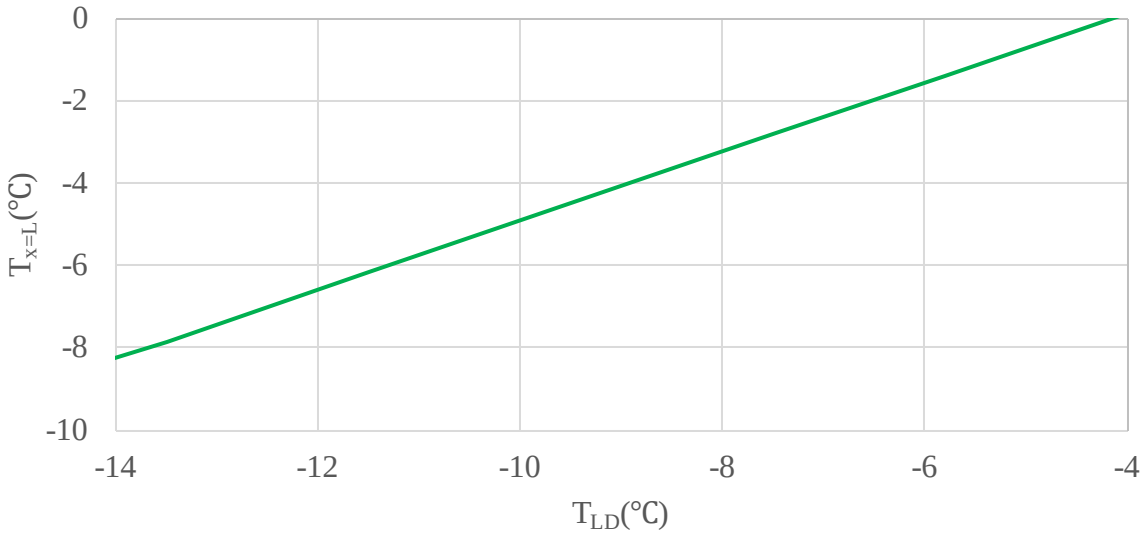

Figure 3.6: Numerical temperature of the top surface of the membrane under steady-state conditions when $RH_{AIR} = 20\%$.

3.7.2 Frosting limit

Figure 3.7 directly compares the analytical frosting limit for the impermeable plate and the permeable membrane. At a constant air relative humidity, a colder liquid desiccant temperature is required to reach saturation conditions in the membrane than on the impermeable plate. For example, if $RH_{AIR} = 20\%$, saturation occurs when $T_{LD} = -6$℃ for the impermeable plate and T_{LD} =-13℃ for the permeable membrane. Thus, the frosting limit is about 7℃ lower for the permeable membrane than for the impermeable plate. Moisture transfer through the permeable membrane reduces the frosting limit. Similarly, moisture transfer through the permeable membrane increases the allowable humidity of the air by about 10% RH.

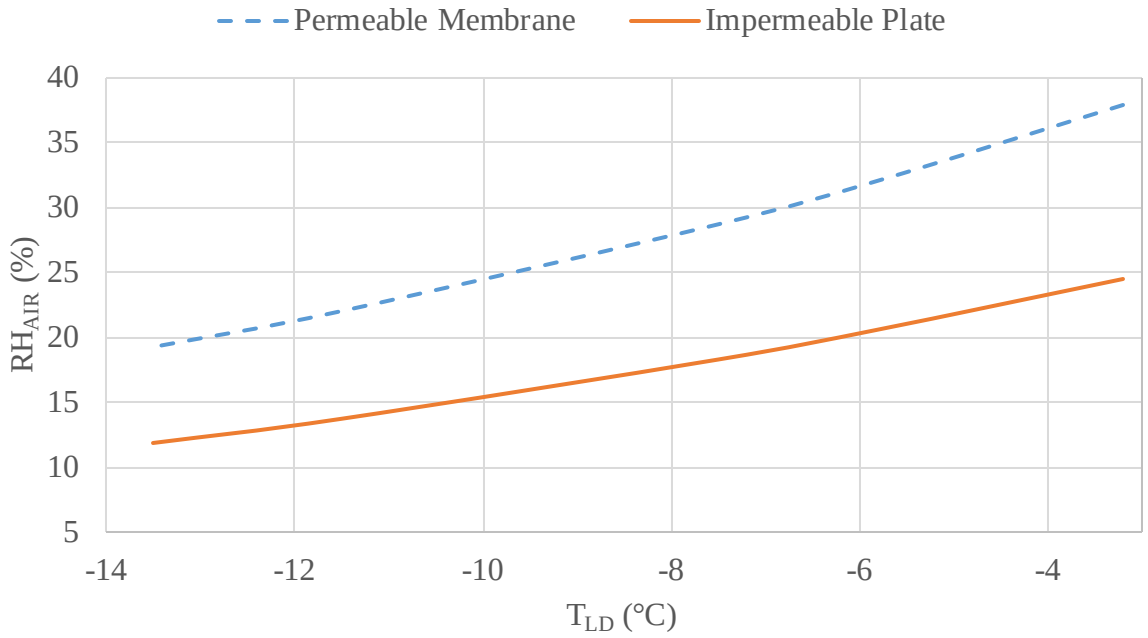

Figure 3.7: Analytical frosting limit for the impermeable plate and the permeable membrane. Frosting will occur for conditions above the line in the graph, while no frosting will occur for conditions below the line.

3.7.3 Sensitivity analysis

The purpose of this section is to determine if the frosting limit can be altered by changing the operating and design parameters in Table 3.2. Changing the operating and design parameters can change the moisture transfer through the membrane and alter the frosting limit. However, changing these properties may also change the surface temperature which will affect the dew point. To isolate the thermal and moisture effects, the results will be presented as the difference between the dew point temperature of the air and the surface temperature (ΔDP) (Equation 3.9). $\Delta DP = 0$ for an impermeable plate and $\Delta DP \geq 0$ for a permeable membrane. A higher ΔDP means the membrane is able to withstand at higher air relative humidity before frosting occurs. Figure 3.8 presents ΔDP for the membrane with base properties (Table 3.1) at different liquid desiccant temperatures. The results show that ΔDP varies between 5°C and 6°C as T_{LD} varies between 0°C and -20°C. This means that the surface temperature of the membrane can be 5 to 6°C below the dew point temperature of the air before frosting will occur on the membrane. The rest of the sensitivity studies will be conducted with a liquid desiccant temperature of -10°C ($T_{LD} = -10$°C).

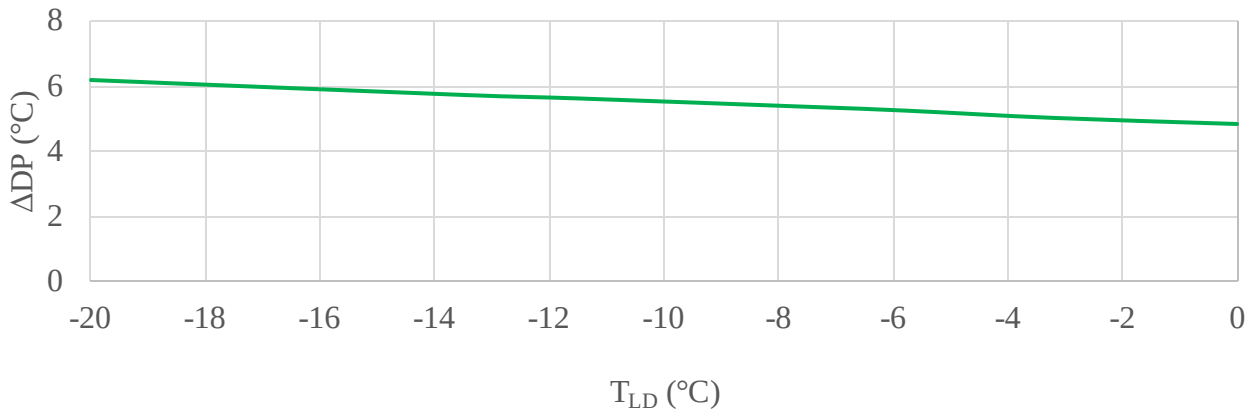

Figure 3.8: The allowable dew point depression of the surface (ΔDP) before saturation (frosting) occurs on the permeable membrane for different liquid desiccant temperatures. Saturation (frosting) will occur for conditions above the line, while there will be no saturation (frosting) for conditions below the line.

3.7.3.1 Diffusion coefficient of the membrane

Figure 3.9 presents allowable dew point depression of the surface (ΔDP) for different diffusion coefficients (D^*) and heat transfer coefficients on the air side ($h^*_{h,AIR}$). As $h^*_{h,AIR}$ changes, the mass transfer coefficient ($h^*_{m,AIR}$) changes as well due to analogy between heat and mass transfer. At a constant heat transfer coefficient on the air side ($h^*_{h,AIR}$), ΔDP increases as D^* increases because the rate of moisture transfer through the permeable membrane increases with D^*. For comparison, the expected values of ΔDP for the permeable membrane tested by Ge et al. (2014) are indicated in Figure 3.9. These results show that membranes can be operated at temperature well below the dew point temperature of the air stream before frosting occurs.

3.7.3.2 Heat transfer coefficient of air side

Figure 3.9 shows that at a constant diffusion coefficient (D^*), ΔDP decreases as the heat transfer coefficient on air side ($h^*_{h,AIR}$) increases. It should be noted when $h^*_{h,AIR}$ increases, the heat transfer from the air to the liquid desiccant increases which increases the sensible effectiveness of the exchanger. When $h^*_{h,AIR}$ increases, the surface temperature at the membrane increases, which would reduce the risk of frost formation. However, as $h^*_{h,AIR}$ increases, the mass transfer coefficient ($h^*_{m,AIR}$) increases as well due to analogy between heat and mass transfer. Increasing

$h^*_{m,AIR}$, increases the vapor density at the surface of the membrane and increases risk of frost formation. Therefore, ΔDP decreases when $h^*_{h,AIR}$ and $h^*_{m,AIR}$ increase (Figure 3.9).

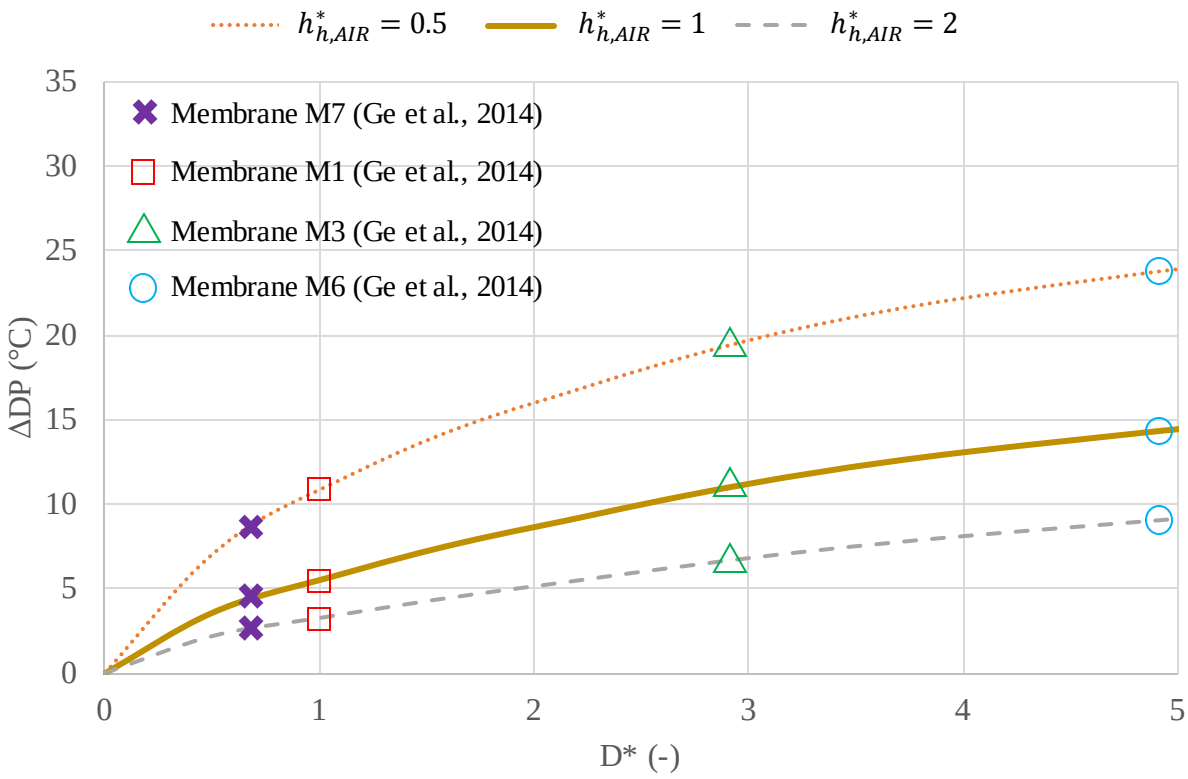

Figure 3.9: Allowable dew point depression of the surface point for different diffusion coefficient and heat transfer coefficient on air side. The predicted dew point depression for membranes tested by Ge et al. (2014) are shown for comparison.

3.7.3.3 Heat transfer coefficient on liquid desiccant side

Figure 3.10 presents ΔDP for different diffusion coefficients (D^*) and heat transfer coefficient on the liquid desiccant side ($h^*_{h,LD}$). At a constant D^*, ΔDP decreases as $h^*_{h,LD}$ increases. Figure 3.10 shows that $h^*_{h,LD}$ has a much smaller effect on ΔDP compared to the effect of D^* and $h^*_{h,AIR}$ on ΔDP. The effect of $h^*_{h,LD}$ is small because the moisture transfer resistance for liquid desiccant side is negligible. If D^*, $h^*_{h,AIR}$ or $h^*_{h,LD}$ change to zero (no moisture transfer), ΔDP becomes zero (Figure 3.9 and 3.10).

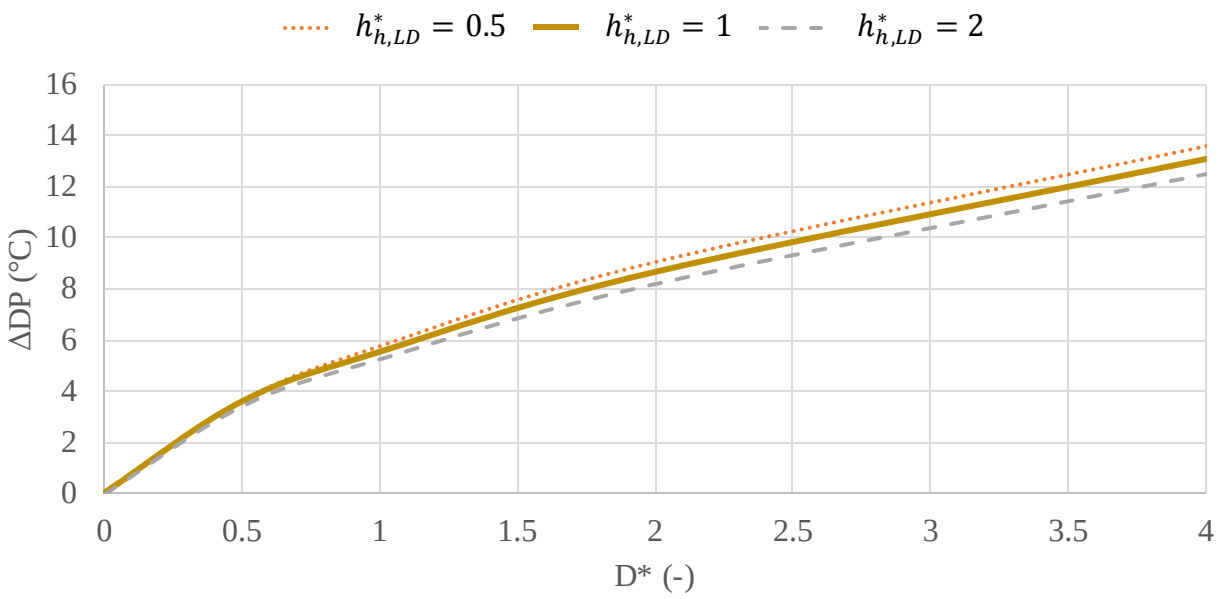

Figure 3.10: Allowable dew point depression of the surface for different diffusion coefficient and heat transfer coefficient on liquid desiccant side.

3.7.3.4 Thickness of the membrane

Figure 3.11 presents ΔDP for different membrane thicknesses (L^*) and diffusion coefficients (D^*). Decreasing the thickness of the membrane (L^*), increases ΔDP. A thin membrane is less susceptible to frosting. When thickness decreases, the top surface temperature of the membrane decreases which will increase the risk of frost formation. However, decreasing the thickness of the membrane increases the moisture transfer rate through the membrane for a constant D^*, which reduces the risk of frost formation (saturation). Since the heat transfer resistance of the membrane ($R_{h,mem}$) is a very small fraction (0.7%) of the total heat transfer resistance, while moisture transfer resistance of the membrane ($R_{m,mem}$) is a large fraction (57.8%) of total moisture transfer resistance ($R_{m,tot}$), changing L^* has a large impact on the moisture transfer than on the heat transfer. As a result, decreasing L^* increases ΔDP which means the membrane is less susceptible to frosting. It should be noted that when thickness of the membrane reduces, it may affect the diffusion coefficient.

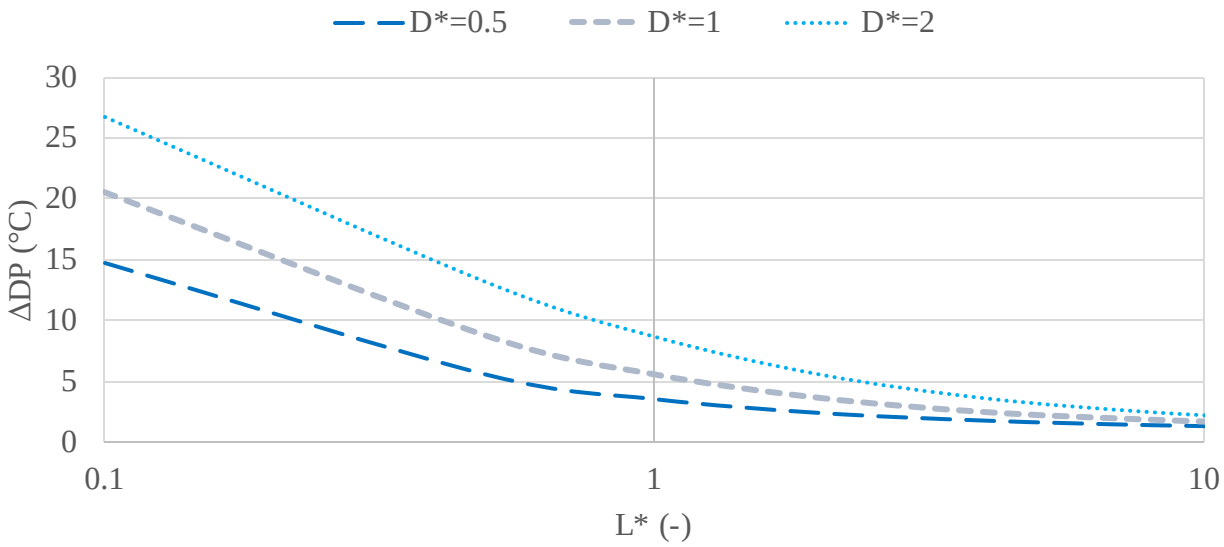

Figure 3.11: Allowable dew point depression of the surface for different thickness of the membrane.

3.7.3.5 Liquid desiccant concentration

Figure 3.12 presents allowable dew point depression of the surface (ΔDP) for different liquid desiccant concentration (C^*) and diffusion coefficients (D^*). For a specific diffusion coefficient (D^*), as concentration of liquid desiccant (C^*) increases, ΔDP increases. Because as C^* increases, the water vapor gradient increases which increases the moisture transfer rate.

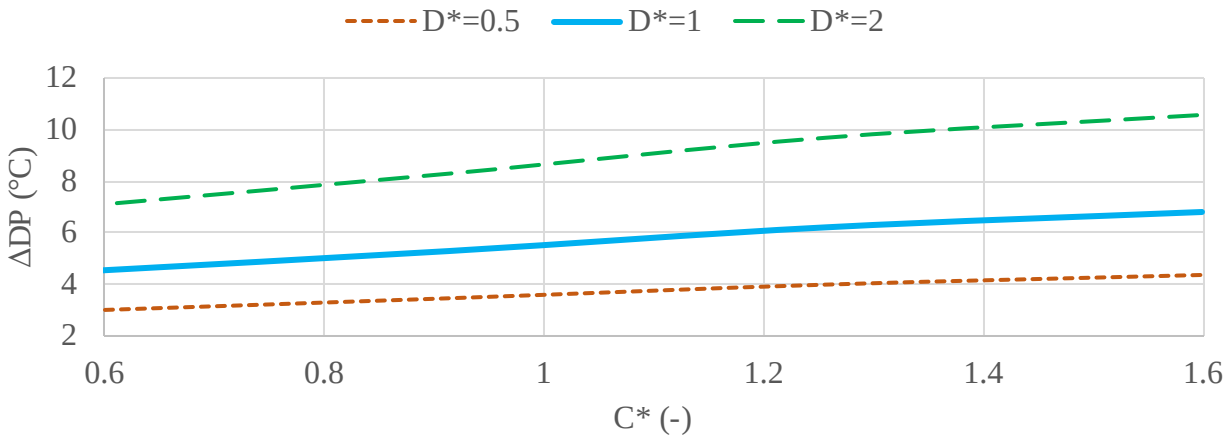

Figure 3.12: Allowable dew point depression of the surface for different concentrations of liquid desiccant.

3.7.3.6 Thermal conductivity of the membrane

Figure 3.13 shows that changing the thermal conductivity of the membrane (k^*) has a negligible effect on ΔDP. The reason for this negligible effect is that the thermal resistance of the membrane is small compared with thermal resistance on air side and liquid desiccant side.

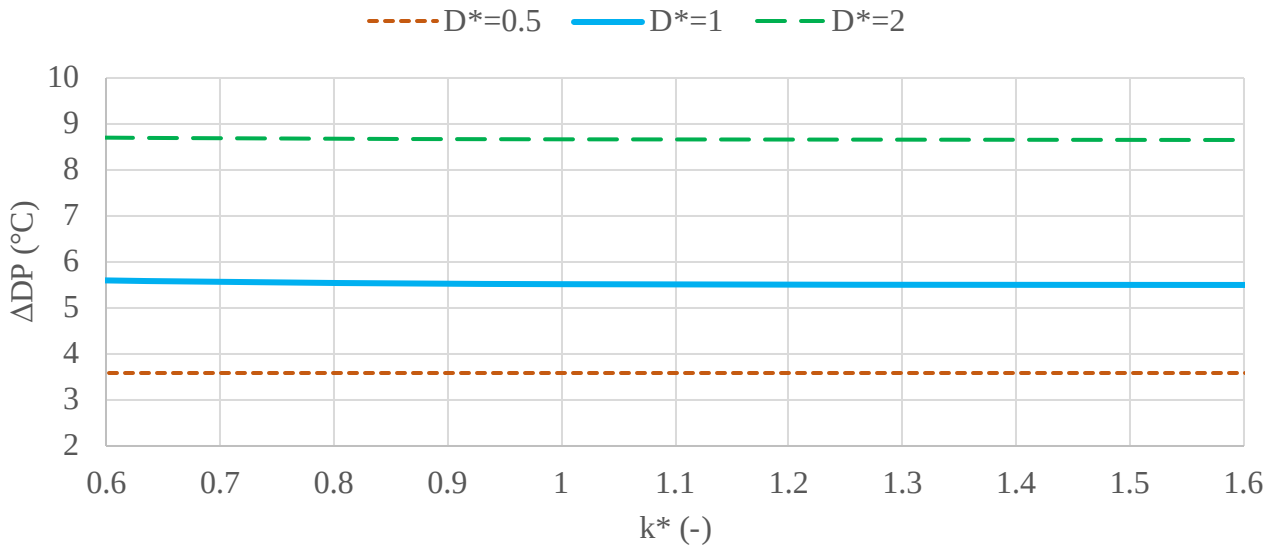

Figure 3.13: Allowable dew point depression of the surface in different thermal conductivity of the membrane.

3.7.3.7 Effect of each parameter on allowable dew point depression of the surface

Figure 3.14 shows that the derivative of allowable dew point depression of the surface (ΔDP) for each variable at the point of the base variables. The derivative compares the magnitude and direction of the changes in each parameter on ΔDP prior to frosting. Increasing the diffusion coefficient of the membrane and the liquid desiccant concentration increase ΔDP. On the other hand, increasing the membrane thickness and the heat transfer coefficient on air side decrease ΔDP. Changing the heat transfer coefficient on liquid desiccant side, thermal conductivity of the membrane and liquid desiccant temperature have a small impact on ΔDP.

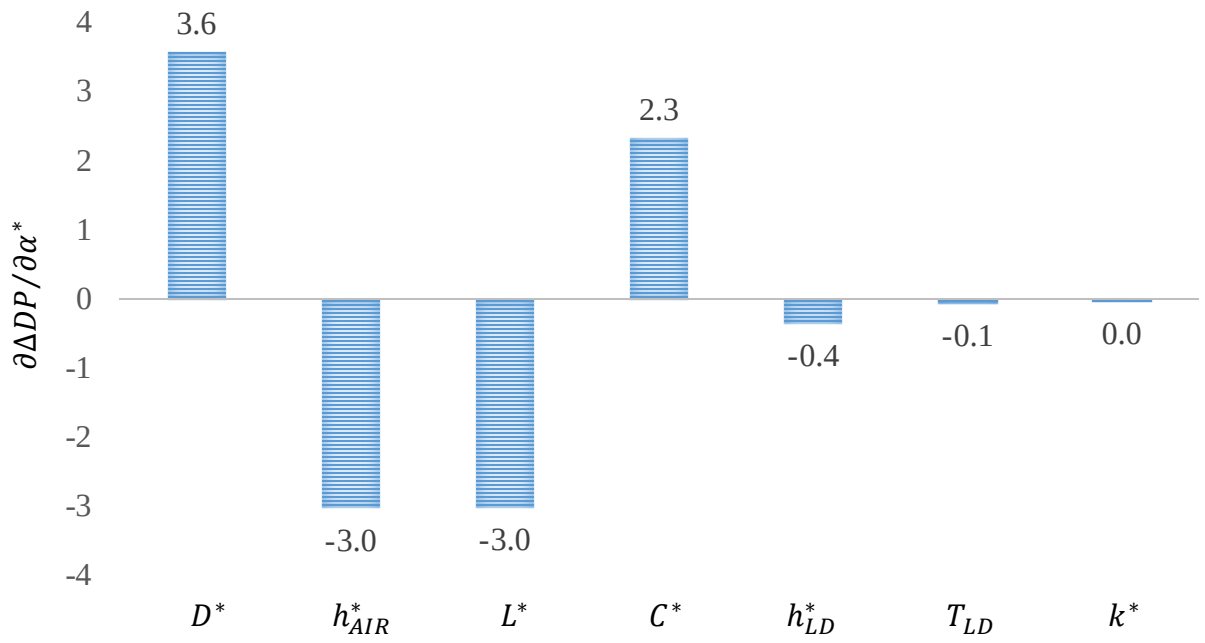

Figure 3.14: Derivative of allowable dew point depression of the surface for each variable at the point of the base variables.

3.7.4 Saturation location

As mentioned previously, saturation occurs at the top surface of the membrane. However, the saturation location depends on the thickness and diffusion coefficient of the membrane. The purpose of this section is to show how the thickness and diffusion coefficient of the membrane affect the place where saturation conditions first occur in the membrane. Therefore, eleven thermal and moisture resistances are defined inside the membrane to calculate relative humidity inside the membrane. Figure 3.15 presents the saturation location inside the permeable and impermeable membrane for different thicknesses and diffusion coefficients of the membrane for the case where the $T_{LD} = -20℃$ and $RH_{AIR} = 50\%$ (other parameters are as listed in Tables 2.1 and 3.1). For comparison, the saturation location for a fiberglass insulation slab which is impermeable at the cold surface tested by Simonson (1993) is indicated in Figure 3.15. Saturation always occurs at top surface of the membrane ($x = L$, air side) when the thickness of the membrane is small (less than 1cm). As thickness and diffusion coefficient of the membrane increase, the saturation location moves toward the bottom surface ($x = 0$).

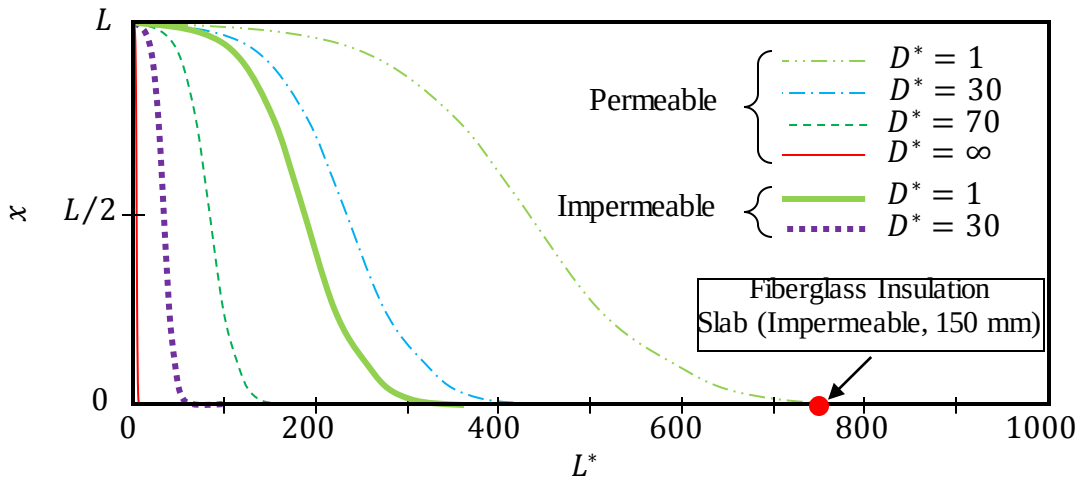

Figure 3.15: Saturation location inside the permeable and impermeable membranes for different thickness and diffusion coefficients of the membranes.

3.8 Conclusion

In this chapter, an analytical heat and mass transfer resistance model has been developed and verified with experimental data to investigate the possibility of avoiding frost in membranes. The analytical and experimental results for the frosting limit show that moisture transfer through the membrane can postpone frost formation. A new parameter, allowable dew point depression of the surface (ΔDP), is defined as the difference between the dew point temperature of the air stream and the temperature at the top surface of the membrane. Sensitivity analyses of ΔDP show that the design and operating parameters which increase the moisture transfer rate through the permeable membrane delay frost formation in membranes. Finally, it has been shown that for thin membranes, saturation (and frosting) occurs on the warm side of the membrane while for thick porous beds (such as fiberglass insulation in typical homes) saturation (and frosting) will occur on the cold side of the porous bed.

CHAPTER 4

SUMMARY, CONCLUSIONS, AND RECOMMENDATIONS

4.1 Summary

The main goal of this thesis was to investigate the possibility of creating a frost-free exchanger by avoiding saturation conditions inside a membrane because saturation is essential for frosting. The hypothesis of this research was that it is feasible to achieve a frost-free exchanger with a vapor permeable membrane. Three objectives were defined to meet the main goal of this thesis:

1. Develop a numerical model for heat and moisture transfer in a vapor permeable membrane to determine when the air in the membrane becomes saturated,
2. Verify the numerical model with experimental data,
3. Investigate the effects of design and operating parameters on the onset of saturation in the membrane.

A numerical model was developed in this thesis to determine temperature and humidity inside a membrane. The developed numerical model was a one-dimensional porous media model based on the theory of local volume averaging and local thermal equilibrium. The goal of the numerical model was to predict the location and time of saturation to prevent or postpone saturation by controlling the moisture transfer rate through the membrane. The model was verified with experimental data and was used to show the effect of moisture transfer on frosting by comparing the onset of saturation in a permeable and an impermeable plate.

A simplified analytical model was developed in order to study frosting at steady state because the transient time for the membrane was short and moisture transfer through the membrane had a small effect on the time at which frosting occurs. The analytical model was verified with experimental data and was used to show that moisture transfer through the membrane can avoid frosting. The analytical model was used to show a range of membrane properties and operating condition which influence the onset of frosting (or saturation).

4.2 Conclusions

This thesis concluded that moisture transfer through membranes can postpone and even avoid frost formation in energy exchangers in some conditions. The results in this thesis show that it is feasible to achieve a frost-free exchanger with a vapor permeable membrane. Numerical results show that changing the moisture properties of the membrane have a small effect on the time at which frosting occurs. The results show that the temperature and humidity at steady state may be found using a simplified analytical model based on thermal and mass resistance.

The verified analytical model shows that the design and operating parameters which increase moisture transfer through a permeable membrane can delay or prevent frosting in the membrane. The analytical model shows that saturation usually occurs on the side of the membrane with the highest temperature and humidity when the thickness of the membrane is small (less than 1cm).

4.3 Recommendations for future work

The following topics are suggested for future research:

- Develop a numerical model to investigate factors affecting frost nucleation by considering surface phenomena like surface roughness, contamination, hydrophobicity or hydrophilicity of surfaces, and adsorption of water vapor on surfaces (Na and Webb, 2003). Results from this model can help determine how to avoid frosting when the air in membranes becomes saturated or supersaturated.
- Perform techno-economic studies of using different membranes to avoid frost formation. The capital cost of different membrane (including components and installation cost) and operating cost of HVAC systems (including energy cost of HVAC systems when frost forms) can be simulated in building simulation software for different cold climate in order to analyze life-cycle cost.
- Validate the transient time of frost formation from the numerical model with experimental results in order to use this time in different defrosting methods (Rafati Nasr et al., 2014). This predictions may reduce energy consumption in HVAC systems.
- Develop a 3D numerical model of an energy exchanger with the presence of frosting.

- Develop a numerical model that includes desiccant material inside the membrane to reduce the risk of frosting.

REFERENCES

Abdel-Salam A.H., 2015. Novel membrane liquid dessicant system. PhD thesis. Department of Mechanical Engineering, University of Saskatchewan, Saskatoon, SK, Canada.

Abdel-Salam M.R.H., Ge G., Fauchoux M., Besant R.W., Simonson C.J., 2014. State-of-the-art in liquid-to-air membrane energy exchangers (LAMEEs): a comprehensive review, *Renewable and Sustainable Energy Reviews*, **39**, 700-728.

Alonso M.J., Mathisen H.M., Aarnes S.A., Liu P., 2017. Performance of a lab-scale membrane-based energy exchanger, *Applied Thermal Engineering*, **111**, 1244-1254.

Alzahrani S., Mohammad A.W., 2014. Challenges and trends in membrane technology implementation for produced water treatment: A review, *Journal of Water Process Engineering*, **4**, 107-133.

Amer M., Wang C., 2017. Review of defrosting methods, *Renewable and Sustainable Energy Reviews*, **73**, 53-74.

ASHRAE, 2017. Handbook - Fundamentals (SI). *American Society of Heating, Refrigerating and Air-Conditioning Engineers*, Inc., Atlanta.

ASME PTC 19.1-2013, Test Uncertainty, American Society of Mechanical Engineers, New York, NY.

Bergman T.L., Lavine A.S., Incropera F.P., Dewitt D.P., 2011. Fundamentals of heat and mass transfer, *John Wiley & Sons*, Seven edition, USA.

Bhattacharjee C., Saxena V.K., Dutta S., 2017. Fruit juice processing using membrane technology: A review, *Innovative Food Science & Emerging Technologies*, **43**, 136-153.

Borgnakke C., Sonntag R.E., 2012. Fundamentals of thermodynamics, 8th edn, *Wiley Global Education*, Chicago, USA.

Cao Y., Wu Z., Su Y., Xu Z., 2015. Aircraft flight characteristics in icing conditions, *Progress in Aerospace Sciences*, **74**, 62-80.

Cassano A., Conidi C., 2017. Chapter 13 – Integration of membrane technologies into conventional existing systems in the food industry. Book: Bioenergy Systems for the Future: Prospects for Biofuels and Biohydrogen, *Elsevier Science & Technology*, 451-479.

Erb B., 2009. Run-around membrane energy exchanger performance and operational control strategies, MSc. Thesis. Department of Mechanical Engineering, University of Saskatchewan. Saskatoon, SK, Canada.

Fauchoux M., 2012. Design and performance testing of a novel ceiling panel for simultaneous heat and moisture transfer to moderate indoor temperature and relative humidity. PhD thesis. Department of Mechanical Engineering, University of Saskatchewan, Saskatoon, SK, Canada.

Ge G., Mahmood G., Ghadiri Moghaddam D., Simonson C.J., Besant R.W., Hanson S., Erb B, Gibson P.W., 2014. Material properties and measurements for semi-permeable membranes used in energy exchangers, *Journal of Membrane Science*, **453**, 328-336.

Hamm B.S.J., Ambrosi A., Griebeler J.G., Marcilio N.R., Tessaro I.C., Pollo L.D., 2017. Recent advances in the development of supported carbon membranes for gas separation, *International Journal of Hydrogen Energy*, **42**, 24830-24845.

Hemingson H., 2010. The impacts of outdoor air conditions and non-uniform exchanger channels on a run-around membrane energy exchanger. MSc thesis. Department of Mechanical Engineering, University of Saskatchewan, Saskatoon, SK, Canada.

Hong S.J., Lear W.E., Kim, M.S., 2014. Physical characteristics of frost formation in semi-closed cycle turbine engines, *Journal of Mechanical Science and Technology*, **28**, 1581-1588.

Iskra C.R., 2007. Convective mass transfer between a hydrodynamically developed airflow and liquid water with and without a vapor permeable membrane, MSc Thesis, Department of Mechanical Engineering, University of Saskatchewan, SK, Canada.

Jeong C.H., Lee J.B.,Lee S.H.,Lee J., You S.M., Choi C.K., 2016. Frosting Characteristics on Hydrophilic and Superhydrophobic Copper Surfaces, *ASME Journal of Heat Transfer,* **138**, (2), 020913.

Kaviany M., 1995. Principles of heat transfer in porous media, 2nd Edition, New York, Springer.

Kim H., Kim D., Jang H, Kim D.R., Lee K.S., 2016. Microscopic observation of frost behaviors at the early stage of frost formation on hydrophobic surfaces, *International Journal of Heat and Mass Transfer*, **97**, 861-867.

Kim P., Wong T.S., Alvarenga J., Kreder M.J., Adorno-Martinez W.E., Aizenberg J., 2012. Liquid-infused nanostructured surfaces with extreme anti-ice and anti-frost performance, *ACS Nano*, **6**, 6569-6577.

Léoni A., Mondot M., Durier F., Revellin R., Haberschill P., 2016. State-of-the-art review of frost deposition on flat surfaces, *International Journal of Refrigeration*, **68**, 198-217.

Li Y., Li W., Liu Z., Lu J., Zeng L., Yang L., Xie L., 2017. Theoretical and numerical study on performance of the air-source heat pump system in Tibet, *Renewable Energy*, **114**, 489-501.

Liu P., Rafati Nasr M., Ge G., Alonso M.J., Mathisen H.M., Fathieh F., Simonson C., 2016. A theoretical model to predict frosting limits in cross-flow air-to-air flat plate heat/energy exchangers, *Energy and Buildings*, **110**, 404-414.

Mahmood G., Simonson C.J., 2012. Frosting conditions for an energy wheel in laboratory simulated extreme cold weather. *In 7th International Cold Climate HVAC Conference*, November 12-14, 2012 Calgary, Alberta, Canada. p. 9.

Mike P., 2014. Arctic offshore pipeline design and installation challenges, *Arctic Technology Conference*, Houston, TX, United States. 10 February 2014 - 12 February 2014.

Na B., Webb R.L., 2003. A fundamental understanding of factors affecting frost nucleation, *International Journal of Heat and Mass Transfer*, **46**, 3797-3808.

Negrelli S., Cardoso R.P., Hermes C.J.L., 2016. A finite-volume diffusion-limited aggregation model for predicting the effective thermal conductivity of frost, *International Journal of Heat and Mass Transfer*, **101**, 1263-1272.

Oberli L., Caruso D., Hall C., Fabretto M., Murphy P.J., Evans, D., 2014. Condensation and freezing of droplets on superhydrophobic surfaces, *Advances in Colloid and Interface Science*, **210**, 47-57.

Parent O., Ilinca A., 2011. Anti-icing and de-icing techniques for wind turbines: Critical review, *Cold Regions Science and Technology*, **65**, 88-96.

Rafati Nasr M., 2016. Frosting in membrane energy exchangers. PhD thesis. Department of Mechanical Engineering, University of Saskatchewan, Saskatoon, SK, Canada.

Rafati Nasr M., Fauchoux M., Besant R.W., Simonson C.J., 2014. A review of frosting in air-to-air energy exchangers, *Renewable and Sustainable Energy Reviews*, **30**, 538-554.

Rafati Nasr M., Kassai M., Ge G., Simonson C.J., 2015. Evaluation of defrosting methods for air-to-air heat/energy exchangers on energy consumption of ventilation, *Applied Energy*, **151**, 32-40.

Rahimi M., Afshari M., Fojan P., Gurevich L., 2015. The effect of surface modification on initial ice formation on aluminum surfaces, *Applied Surface Science*, **355**, 327-333.

Rohsenow M.W., Hartnett J.P., Cho Y.I., 2007. Handbook of heat transfer, *McGraw-Hill*, New York, USA.

Shang W., Chen H., Besant R.W., 2005. Frost Growth in Regenerative Wheels, *Heat Transfer*, **127**, 1015-1026.

Simonson C.J., 1993. Moisture within fiberglass insulation. MSc thesis. Department of Mechanical Engineering, University of Saskatchewan, Saskatoon, SK, Canada.

Sirkar K.K., 2000. Application of membrane technologies in the pharmaceutical industry, *Journal of Current Opinion in Drug Discovery & Development*, **3**, 714-722.

Sommers A.D., Truster N.L., Napora A.C., Riechman A.C., Caraballo E.J., 2016. Densification of frost on hydrophilic and hydrophobic substrates – Examining the effect of surface wettability, *Experimental Thermal and Fluid Science*, **75**, 25-34.

Talukdar P., Iskra C.R., Simonson C.J., 2008. Combined heat and mass transfer for laminar flow of moist air in a 3D rectangular duct: CFD simulation and validation with experimental data, *International Journal of Heat and Mass Transfer*, **51**, 3091-3102.

Talukdar P., Osanyintola O.F., Olutimayin S.O., Simonson C.J., 2007. An experimental data set for benchmarking 1-D, transient heat and moisture transfer models of hygroscopic building materials, *International Journal of Heat and Mass Transfer*, **50**, 4915-4926.

Tassou S.A., Datta D., Marriott D., 2001. Frost formation and defrost control parameters for open multideck refrigerated food display cabinets, *Journal of Power and Energy*, **215**, 213-222.

Wu X., Ma Q., Chua F., Hu S., 2016. Phase change mass transfer model for frost growth and densification, *International Journal of Heat and Mass Transfer*, **96**, 11-19.

Yu C.L., Liu Y.M., Chen G.L., Gu X.H., Xing W.H., 2011. Pretreatment of isopropanol solution from pharmaceutical industry and pervaporation dehydration by NaA zeolite membranes, *Chinese Journal of Chemical Engineering*, **19**, 904-910.

Zhuang D., Ding G., Hu H., Fujino H., Inoue S., 2015. Condensing droplet behaviors on fin surface under dehumidifying condition: Part I: numerical model, *Applied Thermal Engineering*, **105**, 336-344.

APPENDIX A

THE LOCAL VOLUME AVERAGING AND LOCAL THERMAL EQUILIBRIUM TECHNIQUES

This appendix presents the methods used to model a porous media in Chapter 2. The local volume averaging technique (LVA) is a method that can be used to solve governing equations for heat and moisture transfer in porous media and will be used in this thesis (Kaviany, 1991).

In LVA, local properties and equations are averaged over a representative elementary volume (REV). REV is the smallest volume over which a property can be determined that will result in a value representative of the whole system. Kaviany (1991) summarized the theory of heat and mass transfer in porous media. Membranes are porous media. Figure A.1 shows the schematic of a membrane and a representative elementary volume of the membrane. The diameter of membrane fibers (d) is smaller than representative elementary volume of characteristic length (l) which is smaller than the thickness of the membrane (L) (Figure A.1).

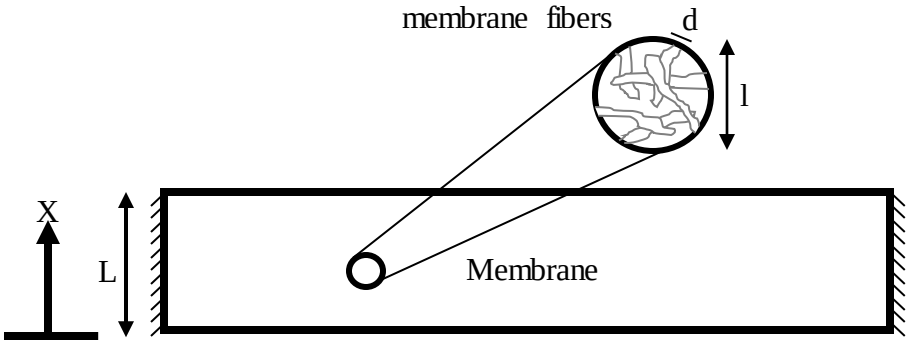

Figure A.1: Schematic of a membrane and representative elementary volume.

In order to implement a local volume averaging technique, the following equation should be satisfied (Kaviany, 1995):

$$d < l \ll L \tag{A.1}$$

The problem can be simplified from two energy equations, (one for the solid and one for the fluid), to one energy equation for the porous media, by assuming local thermal equilibrium (LTE). LTE

is valid when the temperature difference across the different length scales satisfies the following relationship:

$$\Delta T_d < \Delta T_l \ll \Delta T_L \tag{A.2}$$

APPENDIX B

THE DISCRETIZED EQUATIONS AND THE COMPUTER SIMULATION PROGRAM

The discretized equations used within the numerical model present in Chapter 2 are given in this appendix. In addition, the computer simulation program that is used in Chapter 2 is given in this appendix.

B.1 Discretized Equation

The finite difference method is used in order to numerically solve the governing equations and boundary conditions that explained the problem in Chapter 2. The central difference scheme is implemented for the spatial nodes within the membrane and the implicit scheme is used for the time derivative. The backward and forward difference schemes are used at the top and bottom boundaries respectively. The discretized governing equations that are used in the numerical model are as follows:

Energy equation:

$$\begin{aligned}&\left(\rho(i,n)c_p(i,n)\right)_{eff}\frac{T(i,n)-T(i,n-1)}{\Delta t}+\dot{m}(i,n)h_{fg}\\&=\left(\frac{k_{eff}(i+1,n)-k_{eff}(i-1,n)}{2\Delta x}\right)\left(\frac{T(i+1,n)-T(i-1,n)}{2\Delta x}\right)\\&+\left(k_{eff}(i,n)\frac{T(i+1,n)-2T(i,n)+T(i-1,n)}{\Delta x^2}\right)\end{aligned} \tag{B.1}$$

Water vapor diffusion equation:

$$\begin{aligned}&\rho_v(i,n)\frac{\varepsilon_g(i,n)-\varepsilon_g(i,n-1)}{\Delta t}+\varepsilon_g(i,n)\frac{\rho_v(i,n)-\rho_v(i,n-1)}{\Delta t}-\dot{m}(i,n)\\&=\left(\frac{D_{eff}(i+1,n)-D_{eff}(i-1,n)}{2\Delta x}\right)\left(\frac{\rho_v(i+1,n)-\rho_v(i-1,n)}{2\Delta x}\right)\\&+\left(D_{eff}(i,n)\frac{\rho_v(i+1,n)-2\rho_v(i,n)+\rho_v(i-1,n)}{\Delta x^2}\right)\end{aligned} \tag{B.2}$$

where

$$D_{eff}(i,n) = \frac{\varepsilon_g(i,n) D_{AB}}{\tau} \tag{B.3}$$

Continuity equation:

$$\frac{\varepsilon_l(i,n) - \varepsilon_l(i,n-1)}{\Delta t} + \frac{\dot{m}(i,n)}{\rho_{frost}} = 0 \tag{B.4}$$

Volume constraint:

$$\varepsilon_g(i,n) + \varepsilon_l(i,n) + \varepsilon_{mem} = 1 \tag{B.5}$$

Properties:

$$\rho_{eff}(i,n) = \varepsilon_g(i,n)\big(\rho_v(i,n) + \rho_{AIR}(i,n)\big) + \varepsilon_l(i,n)\rho_l + \varepsilon_{mem}\rho_{mem} \tag{B.6}$$

$$c_{p_{eff}}(i,n) = \frac{\varepsilon_g(i,n)\big(\rho_v(i,n)c_{p,v} + \rho_{AIR}(i,n)c_{p,AIR}\big) + \varepsilon_l(i,n)\rho_l c_{p,l} + \varepsilon_{mem}(i,n)\rho_{mem}c_{p,mem}}{\rho_{eff}(i,n)} \tag{B.7}$$

$$k_{eff}(i,n) = \varepsilon_g(i,n)\left(\frac{\rho_v(i,n)k_v + \rho_{AIR}(i,n)k_{AIR}}{\rho_v(i,n) + \rho_{AIR}(i,n)}\right) + \varepsilon_l(i,n)k_l + \varepsilon_{mem}k_{mem} \tag{B.8}$$

Thermodynamic relations:

$$p_{AIR}(i,n) = p_g(i,n) - p_v(i,n) \tag{B.9}$$

$$p_{AIR}(i,n) = R_{AIR}\rho_{AIR}(i,n)T(i,n) \tag{B.10}$$

$$p_v(i,n) = R_v\rho_v(i,n)T(i,n) \tag{B.11}$$

$$p_{v,sat}(i,n) = exp\left(\frac{C_1}{T(i,n)} + C_2 + C_3 T(i,n) + C_4 T^2(i,n) + C_5 T^3(i,n) + ln\, T(i,n)\right) \quad \text{(B.12)}$$

$$RH(i,n) = \frac{p_v(i,n)}{p_{v,sat}(i,n)} \quad \text{(B.13)}$$

B.2 Computer Simulation Program

The computer simulation program presented below is written in MATLAB program language.

```
% By: Pooya Navid
% 27 Aug 2017
% Transient / 1D / Temp. Profile / Heat+Mass Trans
% Warm and humid air flows over the top of the membrane/plate
and cold liquid desiccant passes under the bottom of the
membrane/plate under the bottom of the membrane.

clear all
close all
clc
tic

%================================================================
% constant physical parameter
%================================================================
INPUT=xlsread('C:\Users\pon138\Dropbox\PhD\Mcode\input.xlsx','In
put','A5:AA5');

L =INPUT(9);

T1 = 273.15 + INPUT(3) ;        % (K) Top Air Temp.
```

```
T2 = 273.15 + INPUT(1) ;        % (K) Bottom Air Temp.
delT = abs(T1-T2);

RH_a  = INPUT(4)/100;           % Equivalent RH of the LD
RH_a2 = INPUT(2)/100;           % RH of the Air

Cp0_s = 1200;                   % (J/kgK) Specific Heat Capacity
of Reference
Cpz_s = INPUT(11);              % (J/kgK) Specific Heat Capacity
of the Membrane
Cpb_s = INPUT(14);              % (J/kgK) Specific Heat Capacity
of Ice
Cpa_s = INPUT(12);              % (J/kgK) Specific Heat Capacity
of Air @ (-50 ~ 0 C)
Cpv_s = INPUT(13);              % (J/kgK) Specific Heat Capacity
of Water Vapor

k0_s = 0.06;                    % (W/mK) Thermal Conductivity of
Reference
kz_s = INPUT(15);               % (W/mK) Thermal Conductivity of
the Membrane
kb_s = INPUT(18);               % (W/mK) Thermal Conductivity of
Ice
kv_s = INPUT(17);               % (W/mK) Thermal Conductivity of
Water Vapor
ka_s = INPUT(16);               % (W/mK) Thermal Conductivity of
Air

ro0_s = 440;                    % (kg/m3) Density of Reference
roz_s = INPUT(19);              % (kg/m3) Density of the Membrane
rob_s = INPUT(20);              % (kg/m3) Density of Ice
```

```
Ra = 286.9;                    % (J/kgK) Individual Gas Constant
of Air
Rv = 461.5;                    % (J/kgK) Individual Gas Constant
of Water Vapor

hfg = 2500.8E3;                % (J/kg > J=kgm2/s2) Latent heat

alfae0_s=k0_s/(ro0_s*Cp0_s);   % (m2/s) Effective thermal
Diffusivity

D12_s = 0.26E-4;               % (m2/s) diffusion coefficient

tav = INPUT(10);               % (-) Tortuosity of the membrane

h1 = INPUT(7);                 % (W/m2K) Heat Transfer
Coefficient
hm1 = INPUT(8);                % (m/s) Mass Transfer Coefficient

h2 = INPUT(5);                 % (W/m2K) Heat Transfer
Coefficient
hm2 = INPUT(6);                % (m/s) Mass Transfer Coefficient

Pv0_s = 611.2;                 % (Pa) Pressure of the Reference
Ptotal_s = 1.01325E5;          % (Pa) Total pressure
C1 = -5.6745359 * 10^3;
C2 = 6.3925247;
C3 = -9.6778430 * 10^-3;
C4 =  6.2215701 * 10^-7;
C5 =  2.0747825 * 10^-9;
C6 = -9.4840240 * 10^-13;
```

```
C7 = 4.1635019;

C8  = -5.8002206 * 10^3;
C9  =  1.3914993 ;
C10 = -4.8640249 * 10^-2;
C11 =  4.1764768 * 10^-5;
C12 = -1.4452093 * 10^-8;
C13 =  6.5459673 ;


% NOTE THAT "Pv_sat_a_s1" is for range ABOVE 0C and
"Pv_sat_a_s2" is for
% range below 0C.
Pv_sat_a_s1 = exp( C1/T1 + C2 + C3*T1 + C4 * T1^2 + C5 * T1^3 +
C6 * T1^4 + C7 * log(T1));           % (Pa=kg/ms2) Saturation
Pressure Based on T(K) [Range -100 to 0C]
% Pv_sat_a_s1 = exp( C8/T1 + C9 + C10*T1 + C11 * T1^2 + C12 *
T1^3 + C13 * log(T1));                  % (Pa=kg/ms2)
Saturation Pressure Based on T(K) [Range 0 to +200C]

Pv_sat_a_s2 = exp( C8/T2 + C9 + C10*T2 + C11 * T2^2 + C12 * T2^3
+ C13 * log(T2));                   % (Pa=kg/ms2) Saturation
Pressure Based on T(K) [Range 0 to +200C]

%============================================================
% non-dimensional parameter
%============================================================
P1 = rob_s / ro0_s;
P2 = hfg / (Cp0_s * delT);
P3 = delT * Rv * ro0_s / Pv0_s;
P4 = delT * Ra * ro0_s / Pv0_s;
```

```
teta_1 = T1/delT;
teta_2 = T2/delT;
P_total = Ptotal_s / Pv0_s;

ro_z = roz_s / ro0_s;
ro_b = rob_s / ro0_s;
Cp_z = Cpz_s / Cp0_s;
Cp_b = Cpb_s / Cp0_s;
Cp_v = Cpv_s / Cp0_s;
Cp_a = Cpa_s / Cp0_s;
kz = kz_s / k0_s;
kb = kb_s / k0_s;
kv = kv_s / k0_s;
ka = ka_s / k0_s;

D12 = D12_s / alfae0_s;

Bi_h1 = h1 * L / k0_s ;
Bi_m1 = hm1 * L / alfae0_s ;
Bi_h2 = h2 * L / k0_s ;
Bi_m2 = hm2 * L / alfae0_s ;
%=============================================================
% numerical parameter
%=============================================================
iMax = INPUT(21);
nMax = INPUT(22);
dz = 1 /(iMax-1);
dt_s = INPUT(23);
dt = dt_s / ( L^2 / alfae0_s );
conv  = INPUT(24);
relax_T  = INPUT(25);
```

```
relax_Ro = INPUT(26);

%----------------------preallocation of Matrixes----------------
kMax=11;

T_0 = zeros(1,kMax);
T_iMax = zeros(1,kMax);
RH_0 = zeros(1,kMax);
RH_1 = zeros(1,kMax);
RH_L = zeros(1,kMax);
FROST_TIME = zeros(1,kMax);
q_balance = zeros(1,kMax);
m_balance = zeros(1,kMax);
res_T = zeros(1,kMax);
res_Ro = zeros(1,kMax);

%================================================================
% Different Parameters
%================================================================

for k=1:kMax

    if k>=2
        RH_a2(k) = RH_a2(k-1)-0.01;          % RH of the Air
    end

    P_va = RH_a * Pv_sat_a_s1 /Pv0_s;
    P_va2 = RH_a2(k) * Pv_sat_a_s2 /Pv0_s;
    ro_va1 = P_va/(P3 * teta_1);
    ro_va2 = P_va2/(P3 * teta_2);
```

```
ep_b = zeros(iMax,nMax);
ep_g = zeros(iMax,nMax);
ro_v = zeros(iMax,nMax);
ro_g = zeros(iMax,nMax);
ro_a = zeros(iMax,nMax);
ro_eff = zeros(iMax,nMax);
Cp_eff = zeros(iMax,nMax);
k_eff = zeros(iMax,nMax);
D_eff = zeros(iMax,nMax);
teta = zeros(iMax,nMax);
G = zeros(iMax,nMax);
U = zeros(iMax,nMax);
G_old = zeros(iMax,nMax);
time_dim = zeros(1,nMax);
time = zeros(1,nMax);
dDv_dz = zeros(1,iMax);
depg_dt = zeros(1,iMax);
dk_dz = zeros(1,iMax);
RH = zeros(iMax,nMax);
RH_cal = zeros(1,iMax);
RH_old = zeros(1,iMax);
teta_old = zeros(1,iMax);
ro_old = zeros(1,iMax);
Pv = zeros(1,iMax);
Pv_sat = zeros(1,iMax);
ro_v_sat = zeros(1,iMax);
position = zeros(1,iMax);
A = zeros(iMax-1,iMax-1);
R_A  = zeros(1,iMax-1);
B = zeros(iMax-1,iMax-1);
R_B = zeros(1,iMax-1);
```

```
    error_T = zeros(1,iMax);
    error_ro = zeros(1,iMax);

    for n=1:nMax
        time(n) = (n-1)*dt_s;
    end
    for i=1:iMax
        position(i) = dz*(i-1);
    end

%=============================================================
% initial values
%=============================================================
    for i=1:iMax
        teta(i,1) = teta_1;
        ro_v(i,1) = ro_va1;
        RH_old(i) = RH_a;
        RH(i,1) = RH_a;
        ro_old(i)=ro_va1;
        ep_z = INPUT(27);
        ep_g(i,1) = 1-ep_z;
        ep_b(i,1) = 0.0;
        G(i,1) = 0;
        U(i,1) = (0.0303*RH_a^3-0.02938*RH_a^2+0.01629*RH_a);
    end

%=============================================================
%/////////////////////////////////////////////////////////////
% main program
%\\\\\\\\\\\\\\\\\\\\\\\\\\\\\\\\\\\\\\\\\\\\\\\\\\\\\\\\\\\\\
%=============================================================
```

```
    FROST_TIME(k) = 0;
    for n=2:nMax
        if FROST_TIME(k) > 0
            break
        end
    %----------------------initial value for step n-------------

        for i=1:iMax
            teta(i,n) = teta(i,n-1);
            ro_v(i,n) = ro_v(i,n-1);
            ep_g(i,n) = ep_g(i,n-1);
        end

        max_err = 1;
        count_err = 0;
        dummy = 1;
%-----------------------inner loop for specific time------------
        while (max_err) > conv
            for i=1:iMax
                T_s(i,n) = teta(i,n) * delT;
                if T_s(i,n)<=273.15
                    Pv_sat_s(i,n) = exp( C1/T_s(i,n) + C2 +
C3*T_s(i,n) + C4 * T_s(i,n)^2 + C5 * T_s(i,n)^3 + C6 *
T_s(i,n)^4 + C7 * log(T_s(i,n)));     % (Pa=kg/ms2) Saturation
Pressure Based on T(K) [Range -100 to 0C]
                else
                    Pv_sat_s(i,n) = exp( C8/T_s(i,n) + C9 +
C10*T_s(i,n) + C11 * T_s(i,n)^2 + C12 * T_s(i,n)^3 + C13 *
log(T_s(i,n)));                   % (Pa=kg/ms2) Saturation
Pressure Based on T(K) [Range 0 to +200C]
                end
```

```
                Pv_sat(i,n) = Pv_sat_s(i,n) / Pv0_s;
                ro_v_sat(i,n)= Pv_sat(i,n) / (P3 * teta(i,n));
                Pv(i,n) = P3 * ro_v(i,n) * teta(i,n);
                RH(i,n) = Pv(i,n) / Pv_sat(i,n);
            end

            for i=1:iMax
                if RH(i,n)>1
                    RH(i,n)=1;
                    Pv(i,n) = Pv_sat(i,n);
                    ro_v(i,n) = ro_v_sat(i,n);
                end
            end

            ro_dry = mean( mean( ep_z * ro_z + ep_b(i,n) * ro_b
+ ep_g(i,n) * ro_a(i,n) ) );
            for i=1:iMax
                U(i,n)=(0.0303*RH(i,n)^3-
0.02938*RH(i,n)^2+0.01629*RH(i,n));
                G(i,n) = +(U(i,n) - U(i,n-1)) * ro_dry / dt;
            end

            for i=1:iMax
                ep_b(i,n) = ep_b(i,n-1) + G(i,n) * dt / P1 ;
                ep_g(i,n) = 1.0 - ep_b(i,n) - ep_z;
%-------------------------effective parameter-----------------
                Pa = P_total - Pv(i);
                ro_a(i,n) = Pa / (P4 * teta(i,n));
                ro_g(i,n) = ro_a(i,n) + ro_v(i,n);
                ro_eff(i,n)= ep_z * ro_z + ep_b(i,n) * ro_b +
ep_g(i,n) * ro_g(i,n);
```

```
                Cp_g = ( Cp_v * ro_v(i,n) + Cp_a * ro_a(i,n) ) /
ro_g(i,n) ;
                Cp_eff(i,n) = ( ep_z * ro_z * Cp_z + ep_b(i,n) *
ro_b * Cp_b + ep_g(i,n) *ro_g(i,n) * Cp_g ) / ro_eff(i,n);
                k_eff(i,n) = ep_z * kz + ep_b(i,n) * kb +
ep_g(i,n) * ( ro_a(i,n)*ka + ro_v(i,n)* kv ) / ro_g(i,n);
                D_eff(i,n) = ep_g(i,n)/tav * D12;
            end

%-------------------------Temperature field--------------------
            for i=2:iMax-1
                dk_dz(i) = ( k_eff(i+1,n) - k_eff(i-1,n) ) /
(2*dz);
            end
            i =1;
            A(i,i) = -3-2*dz*Bi_h1/k_eff(i,n);
            A(i,i+1) = 4;
            A(i,i+2) = -1;
            R_A(i) = -2*dz*(Bi_h1)/k_eff(i,n)*teta_1;

            i=iMax;
            A(i,i)   = +1+dz*Bi_h2/k_eff(i,n);
            A(i,i-1) = -1;
            R_A(i)   = dz*(Bi_h2/k_eff(i,n))*teta_2;

            for i=2:iMax-1
                A(i,i) = -( 2*k_eff(i,n)/(dz^2) +
ro_eff(i,n)*Cp_eff(i,n)/dt );
                A(i,i+1) = ( dk_dz(i)/(2*dz) + k_eff(i,n)/(dz^2)
);
```

```
                A(i,i-1) = ( -dk_dz(i)/(2*dz) +
k_eff(i,n)/(dz^2) );
                R_A(i) = -P2 * G(i,n) -
(ro_eff(i,n)*Cp_eff(i,n)/dt) * teta(i,n-1);
            end
            T_result = A\R_A';
            for i=1:iMax
                teta(i,n) = teta(i,n)+ relax_T * ( T_result(i) -
teta(i,n) );
            end

%--------property calculation in one loop-------------------
            for i=1:iMax
                T_s(i,n) = teta(i,n) * delT;
                if T_s(i,n)<=273.15
                    Pv_sat_s(i,n) = exp( C1/T_s(i,n) + C2 +
C3*T_s(i,n) + C4 * T_s(i,n)^2 + C5 * T_s(i,n)^3 + C6 *
T_s(i,n)^4 + C7 * log(T_s(i,n)));     % (Pa=kg/ms2) Saturation
Pressure Based on T(K) [Range -100 to 0C]
                else
                    Pv_sat_s(i,n) = exp( C8/T_s(i,n) + C9 +
C10*T_s(i,n) + C11 * T_s(i,n)^2 + C12 * T_s(i,n)^3 + C13 *
log(T_s(i,n)));                  % (Pa=kg/ms2) Saturation
Pressure Based on T(K) [Range 0 to +200C]
                end
                Pv_sat(i,n) = Pv_sat_s(i,n) / Pv0_s;
                ro_v_sat(i,n)= Pv_sat(i,n) / (P3 * teta(i,n));
                Pv(i,n) = P3 * ro_v(i,n) * teta(i,n);
                RH(i,n) = Pv(i,n) / Pv_sat(i,n);
            end
```

```
            for i=1:iMax
                if RH(i,n)>1
                    RH(i,n)=1;
                    Pv(i,n) = Pv_sat(i,n);
                    ro_v(i,n) = ro_v_sat(i,n);
                end
            end

            ro_dry = mean( mean( ep_z * ro_z + ep_b(i,n) * ro_b
+ ep_g(i,n) * ro_a(i,n) ) );
            for i=1:iMax
                U(i,n)=(0.0303*RH(i,n)^3-
0.02938*RH(i,n)^2+0.01629*RH(i,n));
                G(i,n) = +(U(i,n) - U(i,n-1)) * ro_dry / dt;
            end



            for i=1:iMax
                ep_b(i,n) = ep_b(i,n-1) + G(i,n) * dt / P1 ;
                ep_g(i,n) = 1.0 - ep_b(i,n) - ep_z;
%-------------------------effective parameter-----------------
                Pa = P_total - Pv(i);
                ro_a(i,n) = Pa / (P4 * teta(i,n));
                ro_g(i,n) = ro_a(i,n) + ro_v(i,n);
                ro_eff(i,n)= ep_z * ro_z + ep_b(i,n) * ro_b +
ep_g(i,n) * ro_g(i,n);
                Cp_g = ( Cp_v * ro_v(i,n) + Cp_a * ro_a(i,n) ) /
ro_g(i,n) ;
                Cp_eff(i,n) = ( ep_z * ro_z * Cp_z + ep_b(i,n) *
ro_b * Cp_b + ep_g(i,n) *ro_g(i,n) * Cp_g ) / ro_eff(i,n);
```

```
                k_eff(i,n) = ep_z * kz + ep_b(i,n) * kb +
ep_g(i,n) * ( ro_a(i,n)*ka + ro_v(i,n)* kv ) / ro_g(i,n);
                D_eff(i,n) = ep_g(i,n)/tav * D12;
            end


%-------------------vapor density--------------------------------
            for i=2:iMax-1
                dDv_dz(i) = ( D_eff(i+1,n) - D_eff(i-1,n) ) /
(2*dz);
                depg_dt(i) = ( ep_g(i,n) - ep_g(i,n-1) ) / dt;
            end
            i=1;
            B(i,i) = -3-2*dz*Bi_m1/D_eff(i,n);
            B(i,i+1) = 4;
            B(i,i+2) = -1;
            R_B(i) = -2*dz*(Bi_m1/D_eff(i,n))*ro_va1;


            i=iMax;
            B(i,i)   = +1+dz*Bi_m1/D_eff(i,n);
            B(i,i+1) = -1;
            R_B(i)   = dz*(Bi_m2/D_eff(i,n))*ro_va2;

            for i=2:iMax-1
                B(i,i) = -( 2*D_eff(i,n)/(dz^2) + depg_dt(i) +
ep_g(i,n)/dt );
                B(i,i+1) = ( dDv_dz(i) /(2*dz) +
D_eff(i,n)/(dz^2) );
                B(i,i-1) = ( -dDv_dz(i)/(2*dz) +
D_eff(i,n)/(dz^2) );
```

```
            R_B(i) = +G(i,n) - ep_g(i,n) * ro_v(i,n-1)/dt ;
        end
        ro_result = B\R_B';
        for i=1:iMax
            if RH(i,n)<1
                ro_v(i,n) = ro_v(i,n)+ relax_Ro * (
ro_result(i) - ro_v(i,n) );
            end
        end


%-------------------------error estimation----------------------
        for i=1:iMax
            if teta_old(i)~=0 && ro_old(i)~=0
            error_T(i,n) = abs( ( teta_old(i) - teta(i,n) )
);
            error_ro(i,n) = abs( ( ro_old(i) - ro_v(i,n) )
);
            end
        end


        max_err = max(max(error_T(:,n),error_ro(:,n),
res_T_n(:,n),res_Ro_n(:,n)));
        count_err = count_err+1;


        if n>3
            if count_err==dummy*500
                max_err;
                dummy = dummy+1;
```

```
                    if count_err==400
                        pause
                    end
                end
            end
            for i=1:iMax
                teta_old(i) = teta(i,n);
                ro_old(i) = ro_v(i,n);
                G_old(i) = G(i,n);
            end
        end % END for "while loop"

        for i=1:iMax
            RH_old(i) = RH(i,n);
        end
%--------------------------end of inner loop--------------------
        for i=2:iMax-1

            dk_dz(i) = ( k_eff(i+1,n) - k_eff(i-1,n) ) / (2*dz);
            res_t1(i,n)= ( P2 * G(i,n) +
(ro_eff(i,n)*Cp_eff(i,n)/dt) * (teta(i,n) - teta(i,n-1)) ) - (
(dk_dz(i)/(2*dz))*(teta(i+1,n)-teta(i-1,n)) +
k_eff(i,n)/(dz^2)*(teta(i-1,n)-2*teta(i,n)+teta(i+1,n)) ) ;

            dDv_dz(i) = ( D_eff(i+1,n) - D_eff(i-1,n) ) /
(2*dz);
            depg_dt(i) = ( ep_g(i,n) - ep_g(i,n-1) ) / dt;
            res_ro1(i,n)= ( depg_dt(i)*ro_v(i,n) +
ep_g(i,n)/dt*(ro_v(i,n)-ro_v(i,n-1)) - G(i,n) ) - (
dDv_dz(i)/(2*dz)*(ro_v(i+1,n)-ro_v(i-1,n)) +
D_eff(i,n)/(dz^2)*(ro_v(i-1,n)-2*ro_v(i,n)+ro_v(i+1,n)) ) ;
```

```
        end
        res_T_n=max(abs(res_t1));
        res_Ro_n=max(abs(res_ro1));

%-----------------Energy Balance----------------
        q_LD(n)  = h1*(teta_1-teta(1,n))*delT;  % (W/m2K) * K =
(W/m2)
        q_air(n) = h2*(teta_2-teta(iMax,n))*delT;% (W/m2K) * K =
(W/m2)
        m=G*alfae0_s *ro0_s/L^2;
        for i=1:iMax
            q_stored1(i,n) = (-hfg * m(i,n) -
(ro_eff(i,n)*ro0_s*Cp_eff(i,n)*Cp0_s/dt) * ( teta(i,n) -
teta(i,n-1) )*delT ) * L ;   % (J/kg > J=kgm2/s2) * (kg/s.m^3) -
(kg/m3)*(J/kgK)/s*K =
        end
        q_stored = mean(q_stored1);
        q_balance_n(n) = q_LD(n) + q_air(n) + q_stored(n);
%-----------------Mass Balance----------------
        m_LD(n)  = hm1*(ro_va1-ro_v(1,n))*ro0_s;  % (m/s) *
kg/m3 = (kg/sm2)
        m_air(n) = hm2*(ro_va2-ro_v(iMax,n))*ro0_s;% (m/s) *
kg/m3 = (kg/sm2)
        m_stored = mean(m);
        m_balance_n(n) = m_LD(n) + m_air(n) + m_stored(n);
%-----------------------------------------------


    end % END for "Main Loop"
```

```
end % END for "Different Parameters"
%================================================================
%////////////////////////////////////////////////////////////////
% end of main program
%\\\\\\\\\\\\\\\\\\\\\\\\\\\\\\\\\\\\\\\\\\\\\\\\\\\\\\\\\\\\\\\\\\
\\\\\\\\\\
%================================================================


for k=1:kMax
    OUTPUT(k,1)  = RH_a2(k)*100;
    OUTPUT(k,2)  = T_0(k);
    OUTPUT(k,3)  = T_iMax(k);
    OUTPUT(k,4)  = RH_0(k);
    OUTPUT(k,5)  = RH_1(k);
    OUTPUT(k,6)  = RH_L(k);
    OUTPUT(k,7)  = FROST_TIME(k);
    OUTPUT(k,8)  = q_balance(k);
    OUTPUT(k,9)  = m_balance(k);
    OUTPUT(k,10)  = res_T(k);
    OUTPUT(k,11) = res_Ro(k);
end

xlswrite('C:\Users\pon138\Dropbox\PhD\Mcode\input.xlsx',OUTPUT,'
Output','A2:K12')

toc
TIME=toc;
disp(datestr(datenum(0,0,0,0,0,TIME),'HH:MM:SS'))
```

APPENDIX C

THE INVESTIGATION OF THE RELIABILITY OF THE GRID SIZE, TIME STEP, CONVERGENCE, AND RESIDUALS OF THE COMPUTER SIMULATION PROGRAM

A sensitivity analysis is performed to find the appropriate time step, grid size, and convergence criteria to make the solution independent of these parameters. Figure C.1, Figure C.2 and Figure C.3 show the numerical results for the steady-state temperature and vapor density at the top surface of the membrane ($x = L$) as a function of the grid size, time step and convergence criteria respectively. The properties and boundary conditions for the simulation are given in Table 2.1 and Table 2.2 while the liquid desiccant temperature is -10℃ and air relative humidity is 12%. The selected grid and time step size are identified in Figures C.1, C.2 and C.3.

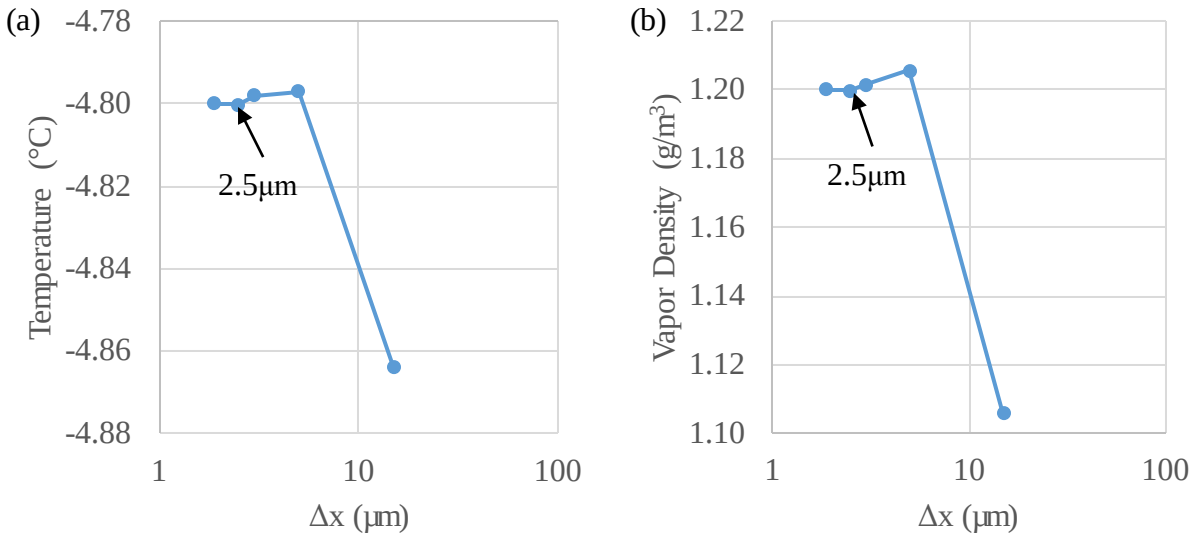

Figure C.1: Sensitivity study showing the effect of the grid size on the (a) temperature and (b) vapor density at the top surface of the member ($x = L$) with $\Delta t = 0.01$s. The selected grid size of 2.5 µm is identified in the figures.

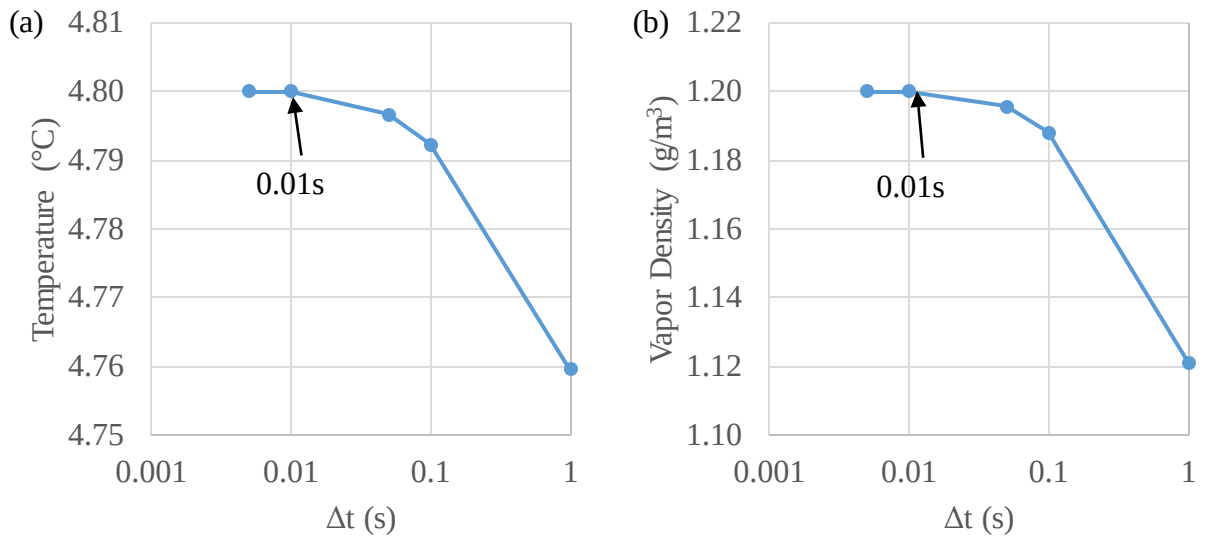

Figure C.2: Sensitivity study showing the effect of the time step on the (a) temperature and (b) vapor density at the top surface of the membrane ($x = L$) with $\Delta x = 2.5\,\mu m$. The selected time step of 0.01s is identified in the figures.

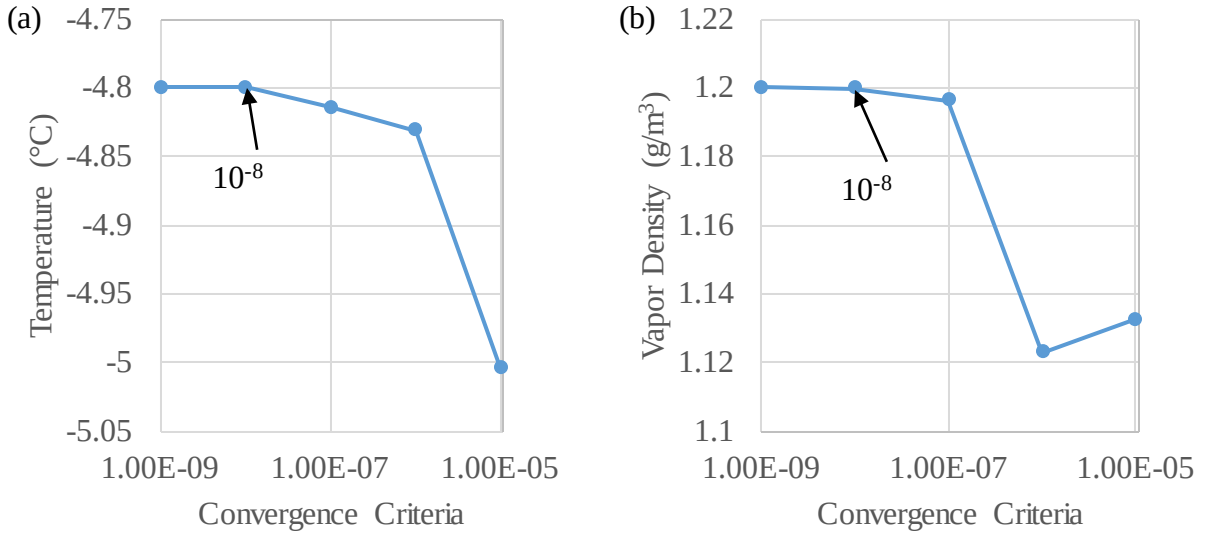

Figure C.3: Sensitivity study showing the effect of the convergence criteria on the (a) temperature and (b) vapor density at top surface of the membrane ($x = L$) with $\Delta t = 0.01$s and $\Delta x = 2.5\,\mu m$. The selected convergence of 10^{-8} is identified in the figures.

Figure C.4 presents the residual of energy and mass balance as a function of time.

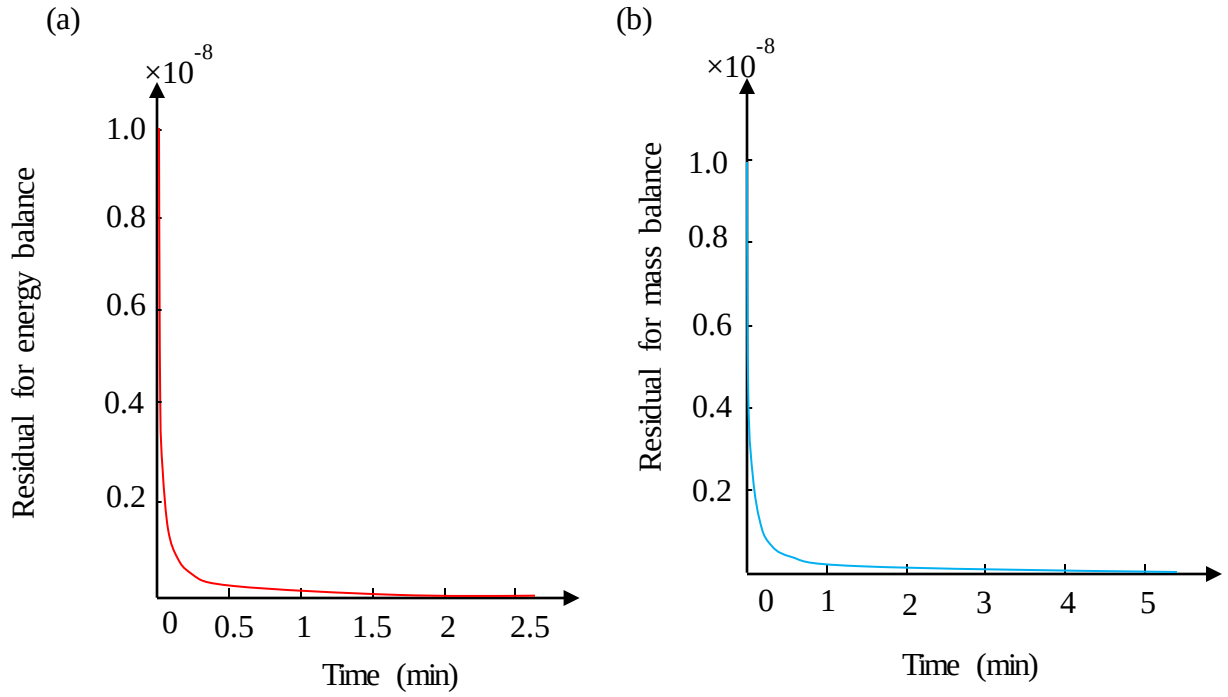

Figure C.4: Residuals of numerical solution for (a) energy balance equations (b) mass balance equations.

APPENDIX D

VERIFICATION OF THE NUMERICAL MODEL WITH AN ANALYTICAL SOLUTION

In this appendix, the numerical model in Chapter 2 is verified with analytical solutions for the case of heat transfer only (no moisture transfer) and for the case of mass transfer only (no heat transfer).

D.1 Heat transfer only (no moisture transfer)

The numerical results are compared with the analytical solution (Bergman et al., 2011) for the case of heat transfer only (no moisture transfer) when a membrane symmetrically cooled by constant surface temperature. Figure D.1(a) presents numerical and analytical transient temperature distributions at the middle of the membrane ($x = L/2$) when surface temperature is constant (17.5℃) and initial temperature is 22℃. Figure D.1(b) presents the error (Equation (2.26)) between numerical and analytical as a function of time. The difference between the numerical and analytical results are usually less than 1%.

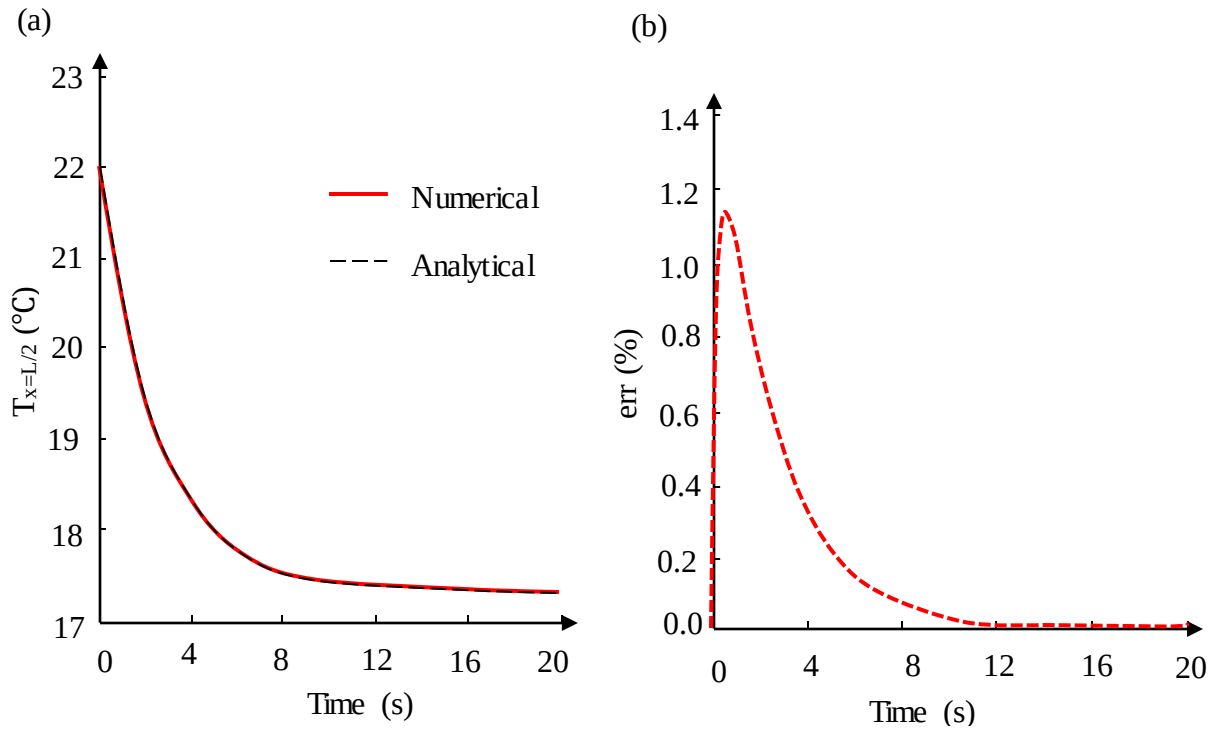

Figure D.1: Verification between numerical and analytical results for the case of heat transfer only (no moisture transfer) (a) temperature distributions (b) error.

D.2 Moisture transfer only (no heat transfer)

The numerical results are compared with the analytical solution (Talukdar et al., 2007) for the case of mass transfer only (no heat transfer) when upper side of a membrane is exposed to a fluid with higher relative humidity but at the same temperature (22°C) as the fluid on the lower side of the membrane. Figure D.2(a) presents numerical and analytical transient vapor density at the top surface of the membrane ($x = L$) when surface relative humidity is 50% and initial relative humidity inside the membrane is 10%. Figure D.2(b) presents the error (Equation (2.27)) between numerical and analytical as a function of time. The difference between the numerical and analytical results are usually less than 1%.

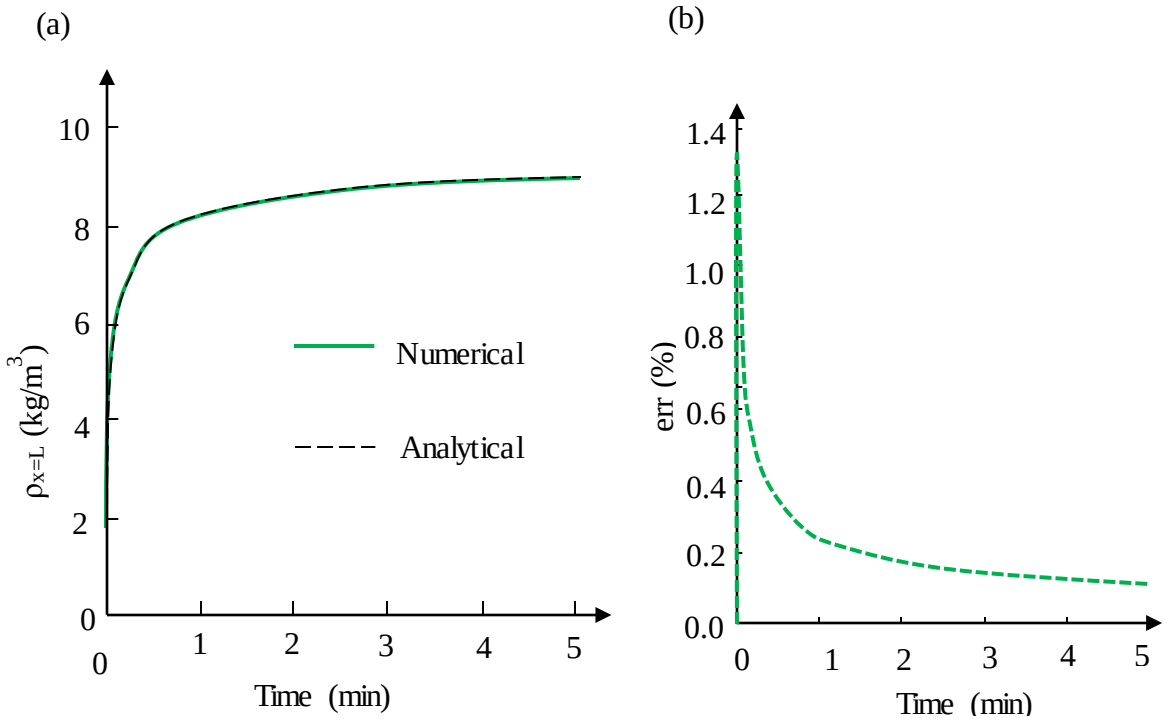

Figure D.2: Verification between numerical and analytical results for the case of moisture transfer only (no heat transfer) (a) vapor density (b) error.